nature communications

Article

https://doi.org/10.1038/s41467-025-62690-1

Obesity-associated macrophages dictate adipose stem cell ferroptosis and visceral fat dysfunction by propagating mitochondrial fragmentation

Received: 16 July 2024

Accepted: 29 July 2025

Published online: 14 August 2025

Check for updates

Yan Tao[1], Jinhao Zang[1], Tianci Wang[1], Peixuan Song[2], Zixin Zhou[1], Huijie Li[1], Yalin Wang[1], Yiyang Liu[1], Haipeng Jie[1,3], Mei Kuang[1], Hui Zhao[4], Fuwu Wang[5], Shen Dai[6], Chun Guo[1], Faliang Zhu[1], Haiting Mao[4], Fengming Liu[1], Lining Zhang[1] & Qun Wang[1]

Morbid obesity induces adipose stem cell (ASC) shortage that impairs visceral adipose tissue (VAT) homeostasis. Macrophages cooperate with ASCs to regulate VAT metabolism, their impact on ASC shortage remains elusive. TNF-α-induced protein 8-like 2 (TIPE2) is an important regulator in immune cells, its expression in VAT macrophages and function in macrophage-ASC crosstalk are largely unknown. Here, TIPE2 loss in VAT macrophages promotes ASC ferroptosis to aggravate diet-induced obesity and metabolic disorders in male mice, which can be corrected by macrophage-specific TIPE2 restoration in VAT. Mechanistically, TIPE2-deficient macrophages propagate mitochondrial fragmentation and reduce delivery of exosomal ferritin toward ASCs, resulting in mitochondrial ROS and Fe^{2+} overload that dictates ASC ferroptosis. TIPE2 interacts with IP3R to constrain IP3R-Ca^{2+}-Drp1 axis, thereby preventing excessive mitochondrial fission and enabling macrophages to protect against ASC ferroptosis. This study reveals distinct obesity-associated macrophages that dictate ASC ferroptosis, and proposes macrophage TIPE2 as therapeutic target for obesity-related diseases.

Morbid obesity, characterized by adipose tissue dysfunction, may lead to insulin resistance, hyperglycemia, and dyslipidemia, thereby increasing the risk of diabetes, fatty liver disease, cardiovascular disease, and even cancer. White adipose tissue (WAT) regulates systemic metabolic balance via fat storage, which integrates a plastic process of adipocyte hyperplasia (increment of newly formed adipocytes) and hypertrophy (enlargement of existing adipocytes). In morbid obesity, an impaired adipogenesis restricts adipocyte hyperplasia while exacerbates adipocyte hypertrophy, which causes pathological remodeling, including inflammation and fibrosis in WAT, particularly visceral WAT (VAT). This WAT dysfunction forces fat accumulation in vital organs, including the liver and heart, resulting in a series of metabolic diseases[1,2]. Adipose stem cells (ASCs) possess high potential for adipogenesis, and thus act as crucial adipocyte precursors in WAT.

[1]Key Laboratory of Infection and Immunity of Shandong Province, Department of Immunology, School of Basic Medical Sciences, Cheeloo College of Medicine, Shandong University, Jinan, China. [2]Department of Statistics, Columbia University, New York, NY, USA. [3]Shandong Provincial Hospital, Cheeloo College of Medicine, Shandong University, Jinan, China. [4]Department of Clinical Laboratory, The Second Hospital, Cheeloo College of Medicine, Shandong University, Jinan, China. [5]Key Laboratory for Experimental Teratology of Ministry of Education, Shandong Key Laboratory of Mental Disorders, Department of Histology and Embryology, School of Basic Medical Sciences, Cheeloo College of Medicine, Shandong University, Jinan, China. [6]Department of Physiology and Pathology, School of Basic Medical Sciences, Cheeloo College of Medicine, Shandong University, Jinan, China. e-mail: wangqun@sdu.edu.cn

Adequate ASCs sustain adipocyte hyperplasia and healthy WAT expansion in response to energy surplus; while ASC shortage in VAT disrupts adaptive adipogenesis, driving pathological adipocyte hypertrophy upon morbid obesity[1,3,4]. Despite cellular senescence that reduces ASC self-renewal[3,4], it remains elusive whether cell death pathway is involved in ASC exhaustion during VAT dysfunction.

Ferroptosis is a form of regulated cell death driven by iron-dependent lipid peroxidation. Intracellular labile divalent iron (Fe^{2+}) can mediate the Fenton reaction to generate reactive oxygen species (ROS) like hydroxyl radicals, which promote peroxidation of unsaturated fatty acids (FAs) in membrane phospholipids. If excessive phospholipid hydroperoxides cannot be reduced by glutathione peroxidase 4 (GPX4), the accumulation of secondary products, including 4-hydroxynonenal (4-HNE) may damage cell membrane and ultimately induce cell death[5,6]. In obese state, VAT often suffers from ROS elevation or iron disorder[7,8]. Mice with genetic obesity had excess iron in epididymal VAT, which was associated with adipocyte hypertrophy, impaired adipogenesis, and metabolic dysfunction. Importantly, iron chelation with deferoxamine (DFO) could effectively reduce adipocyte hypertrophy in VAT, thereby ameliorating obesity and associated insulin resistance in mice[8–10]. These findings provide an insight into iron-elicited impairment in adipogenesis and VAT function, despite a missing link to ASC ferroptosis. Of note, two recent independent clinical studies have suggested a possible involvement of ASC ferroptosis in morbid obesity. WAT from patients with poor outcome in weight management showed high levels of ferroptosis-related genes, including *Acsl4*, the gene encoding acyl-CoA synthase long-chain family member 4 (ACSL4) that dictates ferroptosis[11,12]. This ACSL4 upregulation was verified in epididymal VAT from diet-induced obese mice, accompanied by obvious adipocyte hypertrophy[12]. Importantly, elevated *Acsl4* expression was also observed in ASCs from obese individuals compared to those from non-obese subjects[13], suggesting a potential association between obesity and ASC ferroptosis. So, it is interesting to investigate possible ASC ferroptosis in a high-fat environment, as well as its regulation and metabolic consequences in VAT function. In addition, as the major site of ROS production, mitochondria also play a pivotal role in regulating cell ferroptosis[6]. It is still unclear whether mitochondria regulate ASC fates and related VAT function in obesity.

In lean or obese VAT, macrophages play crucial roles in mediating metabolic homeostasis or disorders. There is growing evidence supporting the interplay between macrophages and ASCs in these processes[14–17]. In lean VAT, alternatively activated M2 macrophages create anti-inflammatory niches to maintain local tissue homeostasis, while ASCs and their exosomes can remodel M2-like macrophages to facilitate inflammation resolution and the beiging process in VAT of obese mice[17–20]. Besides, specific subsets of macrophages may shape the fates of ASCs. For instance, $CD206^{+}$ macrophages in VAT could inhibit the proliferation and adipogenesis of ASCs, thereby affecting adiposity and systemic insulin sensitivity[14]. Our recent study showed that $CX3CR1^{high}$ macrophages remodeled by ASCs could, in turn relieve ASC senescence to drive VAT metabolic adaptation in mice[3]. In obese VAT, M1 (classically activated) macrophage accumulation is considered the primary cause for VAT inflammation and consequent insulin resistance[17,20]. Intriguingly, beyond their well-established proinflammatory effect, macrophages also affect iron distribution in obese VAT[21], thus raising the possibility that VAT macrophages may impact ASC ferroptosis in morbid obesity. If verified, it is important to characterize the distinct phenotypes and regulatory patterns of these macrophages.

In obesity, macrophages accumulated in VAT are generally in activated state, regardless of their phenotypes and subsets. To clarify the fundamental features of these macrophages, we focused on TNF-α-induced protein 8-like 2 (TIPE2), a negative regulator and recently defined checkpoint that regulates multiple immune reactions in addition to inflammation modulation. TIPE2 is predominantly expressed in the spleen and lymph nodes. Its expression in immune cells like T cells, NK cells and macrophages negatively regulates the anti-tumor or anti-infection immune responses by affecting cell maturation, activation, polarization or phagocytosis. Previous studies have shown that TIPE2 can inhibit several signaling pathways including nuclear factor-κB, phosphatidylinositol 3-kinase or mammalian target of rapamycin complex 1 (mTORC1) by targeting Caspase-8 or Rac GTPase[22–26]. More recently, we identified a special role of hepatocyte TIPE2 in driving hepatic gluconeogenesis and preventing hepatic steatosis during fasting, which targeted Raf-1 degradation to inhibit ERK signaling pathway[27]. This prompted us to explore the functions of TIPE2 in VAT metabolism. Interestingly, TIPE2 in immune cells may influence the ferroptosis of other tissue cells, as supported by a recent report showing myocardial cell ferroptosis regulated by TIPE2-deficient T cells in mouse allograft[28]. Given abundant macrophages in VAT, we thus wondered if TIPE2 in VAT macrophages could impact ASC fates, such as ferroptosis in a high-fat condition.

Here, we reveal a causal link between TIPE2 loss in VAT macrophages and ASC ferroptosis. TIPE2 deficiency in macrophages promotes ASC ferroptosis and VAT dysfunction, thereby exacerbating diet-induced obesity and metabolic abnormalities in mice. This vicious process can be alleviated by TIPE2 restoration in VAT macrophages. Mechanistically, TIPE2 deficiency causes excessive mitochondrial fission in macrophages, which propagates mitochondrial fragmentation to ASCs via mitochondrial transfer, ultimately resulting in ROS overload to promote ASC ferroptosis. Furthermore, TIPE2 deficiency disturbs exosomal transfer of ferritin from macrophages into ASCs, resulting in Fe^{2+} overload to increase the susceptibility of ASC ferroptosis.

Results

ASC ferroptosis coincides with TIPE2 loss in VAT macrophages in HFD-fed mice

As morbid obesity increases oxidative stress and iron disorders accompanied by ASC exhaustion in VAT[8,29], we wondered if ASCs were subjected to ferroptosis during obesity-associated VAT dysfunction. We first examined ferroptosis-related lipid peroxidization markers in VAT of the mice fed with a long-term high-fat diet (HFD). Lipofuscin contains oxidative lipids and iron relating to lipid peroxidation and ferroptosis[30]. As determined by autofluorescence, HFD-fed mice showed a significant increase of lipofuscin in VAT compared with normal chow diet (NCD)-fed mice (Fig. 1a). And the final product of lipid peroxidation 4-HNE showed an increase in VAT and ASCs in HFD-fed mice compared with NCD-fed mice (Fig. 1b, c). These observations imply that HFD feeding can increase lipid peroxidation in VAT, particularly in ASCs, in concert with aberrant adipocyte hypertrophy in VAT pathology (Supplementary Fig. 1a). We next examined the key regulators of ferroptosis in VAT of these HFD-fed mice. The pro-ferroptosis protein ACSL4 was remarkably increased in VAT by HFD feeding, especially in ASCs, though anti-ferroptosis proteins cystine transporter solute carrier family 7 member 11 (SLC7A11) and GPX4 showed no obvious decrease (Fig. 1d, e). This imbalance between pro-ferroptosis and anti-ferroptosis regulators in VAT and ASCs indicated a clear tendency toward ferroptosis upon morbid obesity, partially in line with previous studies showing *Acsl4* increase in ASCs or WAT in patients with obesity[12,13]. Furthermore, cleaved Caspase 3, Gasdermin D (GSDMD) and p-MLKL (typical markers for apoptosis, pyroptosis and necrosis) showed no obvious increase in ASCs of VAT from HFD-fed mice (Supplementary Fig. 1b), implying that apoptosis, pyroptosis, and necrosis may not be the primary contributor to ASC shortage. To confirm the sensitivity of ASCs to ferroptosis in the HFD condition, we further examined ferroptosis regulators in primary ASCs that were sorted from mouse VAT. In agreement with the above observations, compared with ASCs of NCD-fed mice, ASCs from HFD-

https://doi.org/10.1038/s41467-025-62690-1

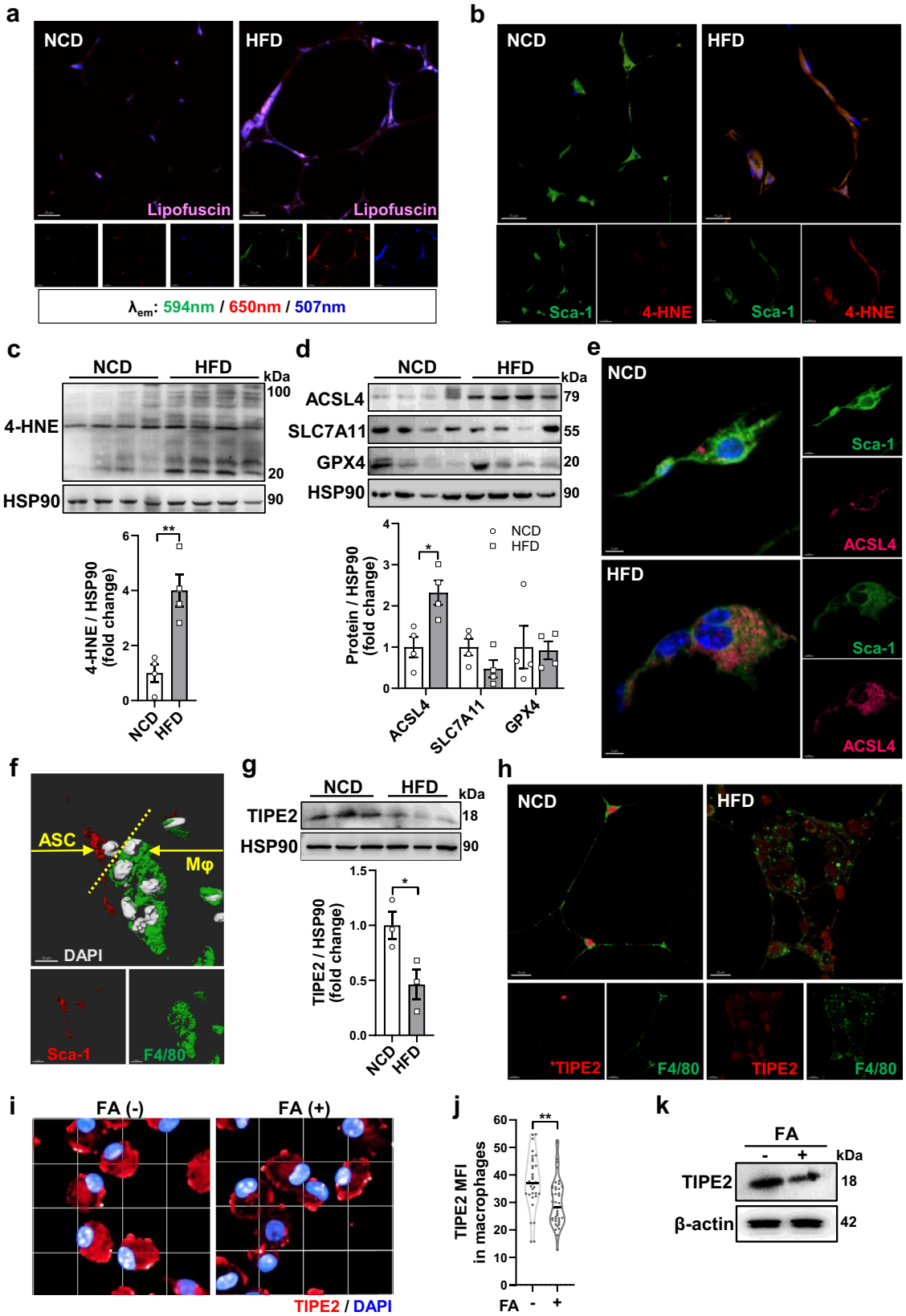

fed mice showed marked increase in ACSL4 protein and no obvious decrease in SLC7A11 and GPX4 proteins, along with an apparent fluorescence shift from non-oxidized to oxidized C11-BODIPY$^{581/591}$, an indicator for ferroptosis-induced lipid peroxidation (Supplementary Fig. 1c–e). Furthermore, regardless of whether the mice were subjected to HFD or not, cleaved Caspase 3, GSDMD and p-MLKL were almost undetectable in their ASCs (Supplementary Fig. 1f), in stark contrast to ACSL4 enrichment in ASCs of HFD-fed mice. These data suggest that VAT ASCs are vulnerable to ferroptosis in morbid obesity, rather than to apoptosis, pyroptosis, or necrosis. Nonetheless, we cannot rule out the potential contribution of alternative cell death pathway to VAT pathology, probably in distinct cell types or environmental cues upon

Fig. 1 | ASC ferroptosis coincides with TIPE2 loss in VAT macrophages in HFD-fed mice. a Representative confocal imaging of lipofuscin autofluorescence in epididymal VAT sections from mice fed with NCD or HFD for 34 weeks. Scale bars, 20 μm. **b** Representative confocal imaging of immunofluorescence for 4-HNE (red) in ASCs (Sca-1, green) in VAT sections. Scale bars, 15 μm. **c, d** Immunoblots and densitometry assay for 4-HNE (**c**), ACSL4, SLC7A11 and GPX4 (**d**) in VAT. $n = 4$ mice per group. **e** Representative confocal imaging of immunofluorescence for ACSL4 (magenta) in ASCs (Sca-1, green) in VAT section. Scale bars, 5 μm. **f** Three-dimensional confocal imaging of spatial adjacency of macrophages (F4/80, green) and ASCs (Sca-1, red) in VAT sections. Scale bars, 10 μm. **g** Immunoblots and densitometry assay for TIPE2 protein in VAT. $n = 3$ mice per group. **h** Representative confocal imaging of immunofluorescence for TIPE2 (red) in macrophages (F4/80, green) in VAT sections. Scale bars, 10 μm. **i–k** Representative immunofluorescence for TIPE2 (red) (**i**) with quantification of mean fluorescence intensity (MFI) (**j**, $n \geq 32$ cells) and TIPE2 immunoblots (**k**) in wild-type macrophages that were treated with or without FA for 18 h, examined over three independent experiments. Scale bars, 20 μm. Three biologically independent samples were examined per condition in (**a**, **b**, **e**, **f**, **h**). Data are presented as mean ± s.e.m. $^{*}P < 0.05$, $^{**}P < 0.01$ determined by two-tailed student's *t*-test (**c**, **d**, **g**, **j**).

obesity. To further ascertain ASC ferroptosis in HFD condition, Ferrostatin-1, a scavenger of lipid peroxidation, was administered into HFD-fed mice. As expected, glucose tolerance and insulin sensitivity were significantly improved by Ferrostatin-1 in these mice, accompanied by the restoration of ASC (Sca-1^{+}CD45^{-}) pool and the reduction of ASC death in VAT (Supplementary Fig. 2a–e).

Given the co-residency of macrophages with ASCs and their interplay in stromal vascular fraction (SVF)[15–17], we wondered if VAT macrophages could influence ASC ferroptosis in long-term HFD-fed mice. Through three-dimensional reconstruction of immunofluorescence images, we notably found a spatial adjacency between macrophages (F4/80^{+}) and ASCs (Sca-1^{+}) in VAT of these mice (Fig. 1f), thus raising the possibility of their intercellular communication. Next, we sought to determine the characteristics of these macrophages in obese VAT. A previous genome-wide analysis proposed TIPE2 as a promising checkpoint of inflammation and metabolism in macrophages[31]. Given large amounts of macrophages in VAT, we first evaluated *Tipe2* expression profile in WAT using public single-cell sequencing data. In both human and mouse WAT, *Tipe2* showed predominant expression in monocyte/macrophage clusters rather than other cell types, including adipocytes and ASCs (Supplementary Fig. 3a, b). In mouse WAT, *Tipe2* was broadly expressed by macrophage subclusters Mac 1–4, which accounted for about 10 percent of each subcluster. And *Tipe2* transcript had slightly higher abundance in Mac 2, Mac 3, and Mac 1, largely due to a rare population of Mac 4 (Supplementary Fig. 3c–e). As compared to several marker genes proposed by previous studies[32], aside from Mac 1 (*Fgf13*) without reported pathway, Mac 2 (*Lyve1*, *Cd163, Plekhg5*), Mac 3 (*Trem2*, *Cd9*, *Lpl*) and Mac 4 (*Prg4*, *Tgfb2*, *Ltbp1*, *Timd4*) were in alignment with previously identified perivascular macrophage (PVM), lipid-associated macrophage (LAM), and regulatory macrophage (RM), respectively (Supplementary Fig. 4a). And immunofluorescence showing TIPE2 protein in Mac 1 (FGF13^{+}), Mac 2 (LYVE1^{+}), Mac 3 (TREM2^{+}) and Mac 4 (TIM4^{+}) further verified TIPE2 expression in these subpopulations (Supplementary Fig. 4b). This indiscriminate *Tipe2* distribution implies a basic and pivotal position of TIPE2 in VAT macrophages. As TIPE2 protein can be degraded upon activation stimuli[33,34], we then detected its protein level in mouse VAT. Surprisingly, TIPE2 protein in VAT is remarkably decreased by long-term HFD (Fig. 1g). Given predominant *Tipe2* expression in macrophages of mouse WAT rather than other cell types, including adipocytes (Supplementary Fig. 3b), the drastic drop of TIPE2 protein in VAT of HFD-fed mice could be largely attributed to the contribution of local macrophages. As expected, further evidence from immunofluorescence verified the decrease of TIPE2 protein in VAT macrophages, although obesity increased the amounts of macrophages (Fig. 1h). These findings indicate that obesity can induce TIPE2 loss in VAT macrophages, probably caused by high-fat microenvironment. Consistently, using FA solution (palmitic acid plus oleic acid) to simulate high-fat setting in obese VAT, we provided evidence that FA treatment markedly reduced TIPE2 protein in primary macrophages, as determined by immunofluorescence and western blot (Fig. 1i–k). Thus, high-fat microenvironment may induce TIPE2 loss in macrophages, coinciding with ASC ferroptosis and VAT abnormality during obesity.

Deficiency of macrophage TIPE2 aggravates obesity and metabolic disorders in HFD-fed mice

To clarify the potential connection of TIPE2 loss in macrophages to ASC ferroptosis during VAT dysfunction, we established HFD-induced obesity in myeloid-specific *Tipe2* knockout (M-*Tipe2*$^{-/-}$) mice. Relative to HFD-fed *Tipe2*$^{flox/flox}$ (M-*Tipe2*$^{+/+}$) mice, these mice showed a dramatic increase in body weight gain independent of food intake; for NCD-fed mice, there was no obvious difference in body weight between the two genotypes (Fig. 2a and Supplementary Fig. 5a, b). Accordingly, HFD-fed M-*Tipe2*$^{-/-}$ mice showed more severe glucose intolerance and insulin resistance than HFD-fed M-*Tipe2*$^{+/+}$ mice, as suggested by higher levels of blood glucose post glucose or insulin administration and corresponding area under the curve (Fig. 2b–e). These findings suggest that macrophage TIPE2 is indispensable for mice to resist severe obesity and associated metabolic dysfunction. Unexpectedly, in HFD condition, TIPE2 deficiency in macrophages led to obvious fat redistribution from VAT to the liver. Compared with HFD-fed M-*Tipe2*$^{+/+}$ mice, HFD-fed M-*Tipe2*$^{-/-}$ mice showed apparent restriction on VAT expansion characterized by smaller and yellower epididymal fat depots and lower ratios of epididymal fat mass to body weight; while both genotypes of mice showed similar expansion of inguinal subcutaneous WAT (SAT) (Fig. 2f–h). More strikingly, the liver from HFD-fed M-*Tipe2*$^{-/-}$ mice showed much larger and yellower morphology than that from HFD-fed M-*Tipe2*$^{+/+}$ mice, together with a higher ratio of liver weight to body weight (Fig. 2f, i). Notably, hepatic lipid contents and Oil Red O staining in liver tissue further confirmed that M-*Tipe2*$^{-/-}$ mice suffered from more severe hepatic steatosis than M-*Tipe2*$^{+/+}$ mice in obese state (Fig. 2j–m). As such, macrophage TIPE2 may act as a fat balancer between adipose tissue and liver, which protects the mice against severe obesity and metabolic dysfunctions including insulin resistance and fatty liver.

Deficiency of macrophage TIPE2 promotes ASC ferroptosis in VAT of HFD-fed mice

To clarify why loss of macrophage TIPE2 restricted VAT expansion in obesity, we next examined the status of VAT and ASCs in these mice. HFD feeding induced obvious adipocyte hypertrophy in both M-*Tipe2*$^{-/-}$ and M-*Tipe2*$^{+/+}$ mice. But differently, VAT from obese M-*Tipe2*$^{-/-}$ mice had significantly larger adipocytes than that from obese M-*Tipe2*$^{+/+}$ mice (Fig. 3a, b), suggesting that TIPE2 depletion in macrophages exacerbates abnormal adipocyte hypertrophy upon obesity. In agreement with this, the expression of adipogenesis genes, including *Pparγ*, *Adiponetin, Cebpα, Pdgfrα,* and *Pdgfrβ* was largely reduced in VAT from obese M-*Tipe2*$^{-/-}$ mice compared with that from obese M-*Tipe2*$^{+/+}$ mice (Fig. 3c, d and Supplementary Fig. 5c). More importantly, PPARγ protein was significantly decreased in VAT of obese M-*Tipe2*$^{-/-}$ mice (Fig. 3e, f), supporting an impairment of adaptive adipogenesis by TIPE2 deficiency in macrophages. Accordingly, compared with HFD-fed M-*Tipe2*$^{+/+}$ mice, HFD-fed M-*Tipe2*$^{-/-}$ mice showed significant increase of 4-HNE in VAT and ASCs, as well as upregulation of lipofuscin in VAT reflected by autofluorescence, particularly in the region of SVF enriched of ASCs (Fig. 3g; Supplementary Fig. 6a). Notably, TIPE2 deficiency in macrophages markedly increased ACSL4 in VAT and ASCs in HFD-fed mice, while had no obvious influence on SLC7A11 and GPX4

https://doi.org/10.1038/s41467-025-62690-1

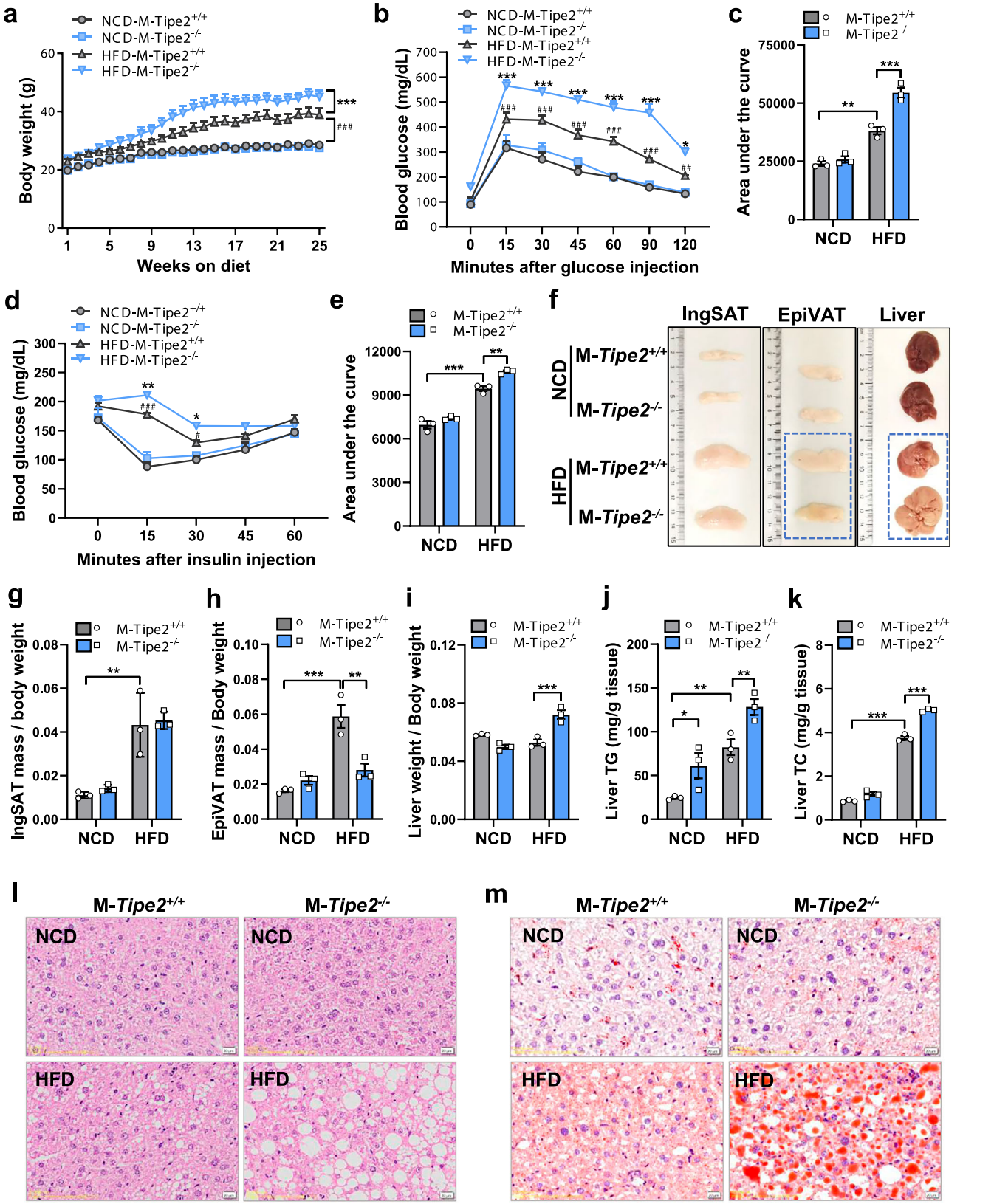

Fig. 2 | Deficiency of macrophage TIPE2 aggravates obesity and metabolic disorders in HFD-fed mice. a–**e** M-*Tipe2*$^{+/+}$ and M-*Tipe2*$^{-/-}$ mice were fed with NCD or HFD for 25 weeks. Body weight change (**a**), glucose tolerance test (**b**) in mice with an overnight fast, insulin tolerance test (**d**) in mice with free access to food, together with corresponding area under the curve (**c, e**). **f-i** Representative images (**f**) of inguinal SAT (IngSAT), epididymal VAT (EpiVAT), liver of the mice, and ratios of IngSAT mass (**g**), EpiVAT mass (**h**), liver weight (**i**) to body weight. **j**–**m** Hepatic triglyceride (TG, **j**) and total cholesterol (TC, **k**) contents, representative H&E staining (**l**) and Oil Red O staining (**m**) in liver sections. Scale bars, 20 μm. $n = 4$ or 5 mice per group (**a**), $n = 3$ mice per group (**b**–**e**, **g**–**k**). Data are presented as mean ± s.e.m. #$P < 0.05$, ##$P < 0.01$, ###$P < 0.001$ (NCD-M-*Tipe2*$^{+/+}$ vs. HFD-M-*Tipe2*$^{+/+}$ in **a**, **b**, **d**); *$P < 0.05$, **$P < 0.01$, ***$P < 0.001$ (HFD-M-*Tipe2*$^{+/+}$ vs. HFD-M-*Tipe2*$^{-/-}$in **a**, **b**, **d**) determined by two-way (a,b,d), one-way ANOVA (c, e, g-k).

https://doi.org/10.1038/s41467-025-62690-1

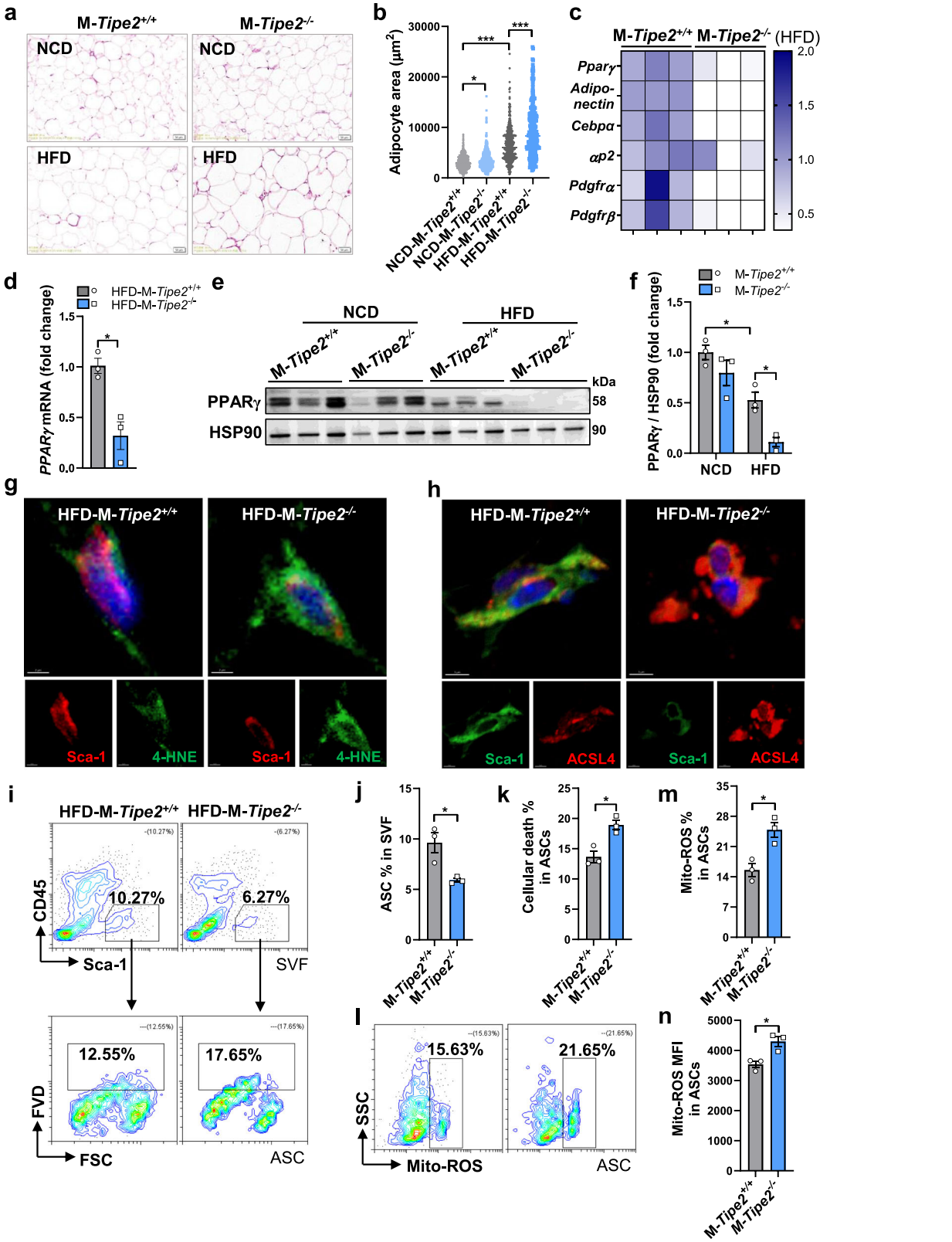

Fig. 3 | Deficiency of macrophage TIPE2 promotes ASC ferroptosis in VAT of HFD-fed mice. a, b Representative images of H&E staining (**a**) and statistical analysis of adipocyte sizes (**b**; $n \geq 395$ adipocytes examined over 3 mice per group) in VAT sections from mice indicated in Fig. 2. Scale bars, 50 μm. **c**–**f** Heat map (**c**) for adipogenesis gene expression, PPAR-γ mRNA (**d**) and protein (**e, f**) levels in epididymal VAT. **g, h** Representative confocal imaging of immunofluorescence for 4-HNE (green) in ASCs (Sca-1, red) (**g**) and ACSL4 (red) in ASCs (Sca-1, green) (**h**) in VAT sections. Scale bars, 2 μm (g) and 5 μm (**h**). **i**–**n** Flow cytometry frequencies of ASCs (Sca-1$^+$CD45$^-$) in SVF (**i, j**), cellular death (**i, k**) and mitochondrial ROS (**l, m**) in ASCs with MFI quantification (**n**) in VAT. $n = 3$ mice per group (**c**, **d**, **f**, **j**, **k**, **m**, **n**). Data are presented as mean ± s.e.m. $^*P < 0.05$, $^{**}P < 0.01$, $^{***}P < 0.001$ determined by one-way ANOVA (**b**, **f**) or two-tailed student's *t*-test (**d**, **j**, **k**, **m**, **n**).

https://doi.org/10.1038/s41467-025-62690-1

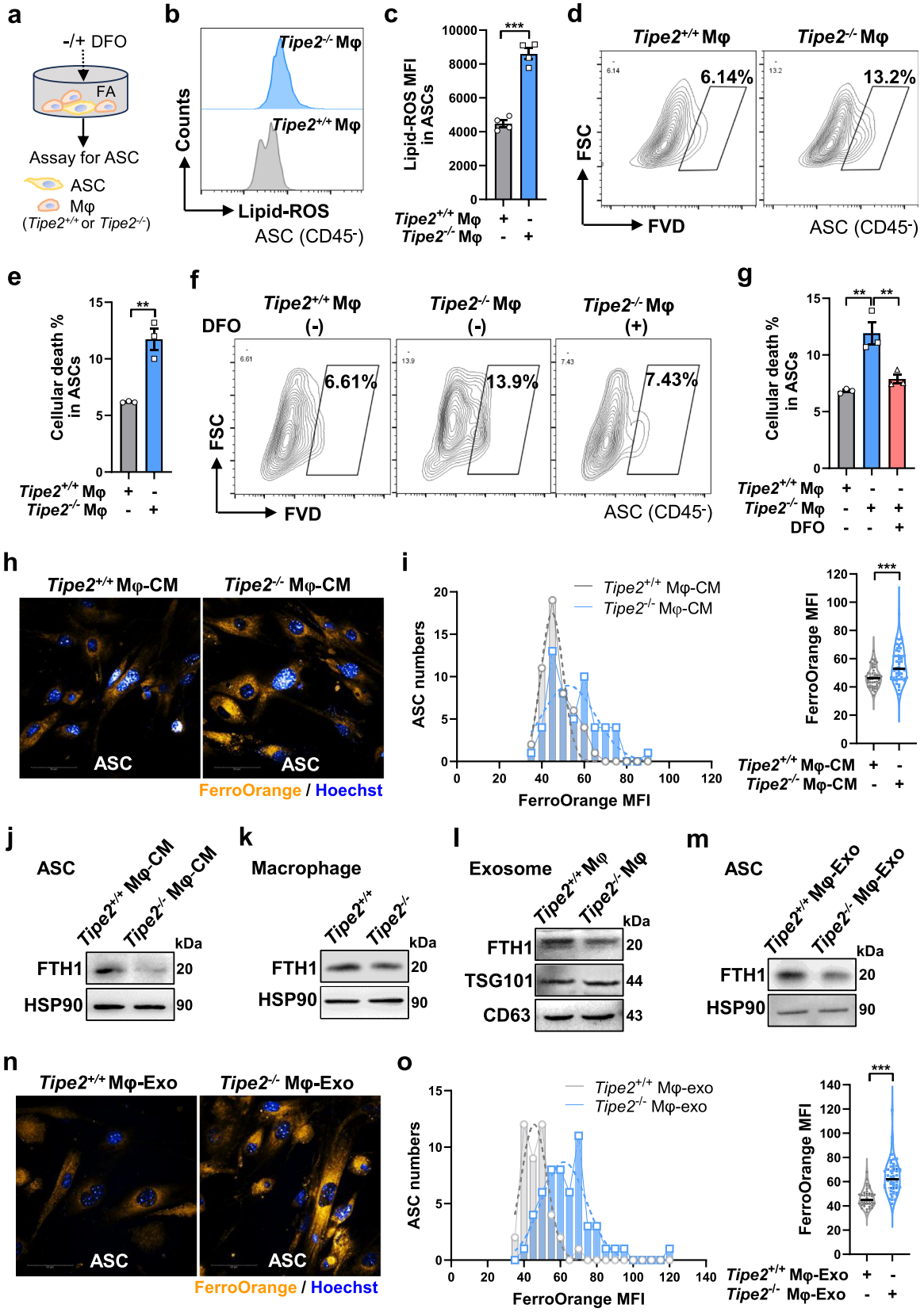

(Fig. 3h; Supplementary Fig. 6b). Furthermore, the accumulation of transferrin receptor 1 (TFR1) into plasma membrane of ASCs was increased in HFD-fed M-*Tipe2*$^{-/-}$ mice compared with HFD-fed M-*Tipe2*$^{+/+}$ mice, together with an abnormal morphology of shrunken mitochondria in transmission electron microscopy (Supplementary Fig. 6c, d). In addition, there was no obvious difference in cleaved Caspase 3, GSDMD, and p-MLKL in ASCs of VAT between HFD-fed M-*Tipe2*$^{-/-}$ and M-*Tipe2*$^{+/+}$ mice (Supplementary Fig. 6e), largely excluding the influence of macrophage TIPE2 deficiency on ASC apoptosis, pyroptosis or necrosis. These observations implied that deficiency of macrophage TIPE2 might induce an activate ferroptosis process in VAT of HFD-fed mice, which was independent of GPX4 inhibition. In agreement with this, ASC

Fig. 4 | TIPE2-deficient macrophages dictate ASC ferroptosis in vitro. **a** Schematic of coculture assay for ASCs (wild-type) and macrophages (*Tipe2*$^{+/+}$ or *Tipe2*$^{-/-}$) in the presence of FA for 24 h. **b, c** Flow cytometry frequency (**b**) of lipid ROS in ASCs (CD45$^-$) with MFI quantification (**c**; $n = 4$) after coculture with *Tipe2*$^{+/+}$ or *Tipe2*$^{-/-}$ macrophages. **d–g** Flow cytometry frequency (**d, e**; $n = 3$) of ASC death after coculture with *Tipe2*$^{+/+}$ or *Tipe2*$^{-/-}$ macrophages, or in the presence of 100 μM DFO (**f, g**; $n = 3$). **h–j** Representative confocal imaging (**h**) of intracellular Fe^{2+} with MFI quantification by ImageJ (**i**; $n \geq 51$ cells examined over two independent experiments) and immunoblots for FTH1 protein (**j**) in ASCs that were incubated with condition medium (CM) from *Tipe2*$^{+/+}$ or *Tipe2*$^{-/-}$ macrophages for 24 h. Scale bars, 50 μm. **k, l** Representative immunoblots for FTH1 protein in *Tipe2*$^{+/+}$ or *Tipe2*$^{-/-}$ macrophages (**k**) and their exosomes (**l**). **m–o** Representative immunoblots for FTH1 protein (**m**) and confocal imaging (**n**) of intracellular Fe^{2+} with MFI quantification by ImageJ (**o**; $n \geq 42$ cells examined over two independent experiments) in ASCs that were incubated with 50 μg exosomes from *Tipe2*$^{+/+}$ or *Tipe2*$^{-/-}$ macrophages for 24 h. Scale bars, 50 μm. Data are presented as mean ± s.e.m. $^{**}P < 0.01$, $^{***}P < 0.001$ determined by two-tailed student's *t*-test (**c, e, i, o**) or one-way ANOVA (**g**). Data are representative of two or three independent experiments.

population was decreased whilst ASC death was increased in VAT of HFD-fed M-*Tipe2*$^{-/-}$ mice relative to HFD-fed M-*Tipe2*$^{+/+}$ mice, together with an elevation of mitochondrial ROS in these ASCs (Fig. 3i–n). In fact, compared to NCD feeding, HFD itself increased ASC death in M-*Tipe2*$^{+/+}$mice, largely due to its contribution to TIPE2 loss in macrophages; even in NCD condition, TIPE2 deficiency in macrophages also caused an increasing trend of ASC death (Supplementary Fig. 6f–h). Nonetheless, the death proportion of ASCs appeared to be in concert with the rapid turnover of SVF, including ASCs in WAT, as reported by previous studies[35–37], probably a kind of adaptive or compensatory reaction. Of note, upon Ferrostatin-1 treatment, HFD-fed M-*Tipe2*$^{-/-}$ mice showed marked improvement in metabolic outcome, accompanied by substantial reduction in ASC death and adipocyte hypertrophy in VAT (Supplementary Fig. 7a–h). Collectively, Deficiency of macrophage TIPE2 may promote ASC ferroptosis, subsequently resulting in VAT dysfunction in HFD-fed mice.

TIPE2-deficient macrophages drive ASC ferroptosis by propagating mitochondria fragmentation

To determine whether macrophage TIPE2 could directly regulate ASC ferroptosis, we cocultured ASCs with *Tipe2*$^{+/+}$ or *Tipe2*$^{-/-}$ macrophages via cell-cell contact in the presence of FA (Fig. 4a), followed by ferroptosis assay using lipid ROS indicator C11-BODIPY$^{581/591}$. In this coculture system, CD45 was used to distinguish macrophages (CD45$^+$, immune cells) and ASCs (CD45$^-$, non-immune cells) by referring to previous studies[38–40]. Compared with *Tipe2*$^{+/+}$ macrophages, *Tipe2*$^{-/-}$ macrophages significantly increased lipid ROS in ASCs (Fig. 4b, c), consequently resulting in an increase of ASC death (Fig. 4d, e). This difference in ASC death was further verified by 7-AAD$^+$ population; whereas both groups showed similar frequencies in Annexin V$^+$ 7-AAD$^-$ population, preliminarily excluding the involvement of apoptosis in ASC death caused by *Tipe2*$^{-/-}$ macrophages (Supplementary Fig. 8a, b). Importantly, the increment of ASC death caused by *Tipe2*$^{-/-}$ macrophages was remarkably abolished by DFO or Ferrostatin-1 (Fig. 4a, f, g; Supplementary Fig. 8c, d), indicating that ASC death elicited by *Tipe2*$^{-/-}$ macrophages is dependent on iron and lipid oxidation. By contrast, the apoptosis/proptosis or necrosis inhibitors z-VAD-FMK or Necrostatin-1 could not significantly reduce ASC death (Supplementary Fig. 8c, d), further ruling out the primary contribution of apoptosis, proptosis, or necrosis to this process. Additionally, upon pretreatment with RSL3, a GPX4 inhibitor, ASC death was substantially induced in *Tipe2*$^{-/-}$ macrophage coculture, which showed a remarkable increase compared with that in *Tipe2*$^{+/+}$ macrophage coculture (Supplementary Fig. 8e, f), further supporting that *Tipe2*$^{-/-}$ macrophages could promote the susceptibility of ASCs to ferroptosis.

Next, we asked whether these macrophages affected iron homeostasis in ASCs. Interestingly, condition medium from *Tipe2*$^{-/-}$ macrophages, relative to that from *Tipe2*$^{+/+}$ macrophages, significantly upregulated intracellular Fe^{2+} but downregulated ferritin heavy chain 1 (FTH1) in ASCs (Fig. 4h–j), indicating that soluble factors from macrophages may mediate their different effects. Given previously identified exosome pathway for ferritin transportation and the role of FTH1 in sequestering iron to reduce Fe^{2+} pool[6,41], we speculated that exosomes from *Tipe2*$^{+/+}$ or *Tipe2*$^{-/-}$ macrophages might produce different influences on the levels of FTH1 protein and Fe^{2+} in ASCs. To this end, *Tipe2*$^{-/-}$ or *Tipe2*$^{+/+}$ macrophages were treated with exosome inhibitor GW4869, and conditioned medium was collected for ASC incubation. Exosome inhibition successfully reduced the difference in the ability of *Tipe2*$^{-/-}$ and *Tipe2*$^{+/+}$ macrophage condition medium to affect the levels of FTH1 protein and Fe^{2+} in ASCs (Supplementary Fig. 9a–c). Thus, the exosome pathway may play a role in regulating FTH1 and Fe^{2+} in ASCs by macrophages. To further ascertain the contribution of exosomes in this process, we examined FTH1 protein in exosomes from the above macrophages. Relative to *Tipe2*$^{+/+}$ macrophages, *Tipe2*$^{-/-}$ macrophages showed a decline in FTH1 protein; in concert with this, exosomes from *Tipe2*$^{-/-}$ macrophages carried much less FTH1 protein than those from *Tipe2*$^{+/+}$ macrophages (Fig. 4k, l and Supplementary Fig. 9d). This indicates that TIPE2 deficiency may reduce ferritin in macrophages and impair their capacity for loading exosomal ferritin. In addition, Prussian blue staining showed that the iron was hardly detectable in exosomal ferritin compared to the source *Tipe2*$^{+/+}$ or *Tipe2*$^{-/-}$ macrophages (Supplementary Fig. 9e). As such, unlike exosomes from *Tipe2*$^{-/-}$ macrophages that carried very little ferritin, exosomes from *Tipe2*$^{+/+}$ macrophages carried abundant ferritin that contained very little iron, at least unsaturated, thus acquiring a potential for iron sequestration to reduce the labile iron pools in target cells. As expected, ASCs treated with *Tipe2*$^{-/-}$ macrophage exosomes showed downregulation in FTH1 protein while upregulation in Fe^{2+} compared with those treated with *Tipe2*$^{+/+}$ macrophage exosomes (Fig. 4m–o). In addition, *Tipe2*$^{+/+}$ macrophage exosomes but not *Tipe2*$^{-/-}$ macrophage exosomes could successfully rescue the downregulation of FTH1 protein in ASCs caused by conditional medium from GW4869-treated *Tipe2*$^{+/+}$ macrophages (Supplementary Fig. 9f). These data demonstrate that TIPE2 deficiency in macrophages may disturb the delivery of exosomal ferritin into ASCs, thereby causing Fe^{2+} overload in ASCs to increase their susceptibility to ferroptosis.

Considering that in vivo depletion of macrophage TIPE2 led to an upregulation of mitochondrial ROS in ASCs of VAT under an obese condition, we then asked whether *Tipe2*$^{-/-}$ macrophages directly affected mitochondrial ROS in ASCs. Remarkably, relative to *Tipe2*$^{+/+}$ macrophages, *Tipe2*$^{-/-}$ macrophages significantly upregulated the levels of mitochondrial ROS in ASCs (Fig. 5a, b); while blockade of mitochondrial ROS with MitoTEMPO markedly abolished the increment of lipid ROS in ASCs that was caused by *Tipe2*$^{-/-}$ macrophages (Fig. 5c, d). In this regard, mitochondrial ROS overload is another critical contributor to ASC ferroptosis. To further ascertain why ASCs in coculture with *Tipe2*$^{+/+}$ or *Tipe2*$^{-/-}$ macrophages had different levels of mitochondrial ROS, we tracked mitochondrial ROS of macrophages through MitoSOX labeling before the coculture. Surprisingly, macrophage-derived mitochondrial ROS was readily detectable in ASCs, while *Tipe2*$^{-/-}$ macrophages rendered more mitochondrial ROS into ASCs than *Tipe2*$^{+/+}$ macrophages (Fig. 5e–g). In agreement with the delivery of mitochondrial ROS, mitochondrial tracking assay showed an apparent mitochondrial transfer from both genotypes of macrophages into ASCs. But differently, mitochondria from *Tipe2*$^{-/-}$ macrophages exhibited obvious fragmentation compared with those from *Tipe2*$^{+/+}$ macrophages, characterized by small and short morphology (Fig. 5h, i). And live-cell imaging further confirmed the mitochondrial transfer from *Tipe2*$^{-/-}$ macrophages into ASCs (Supplementary Fig. 10). It has been recognized that nano-tube tunneling (TNT) is involved in

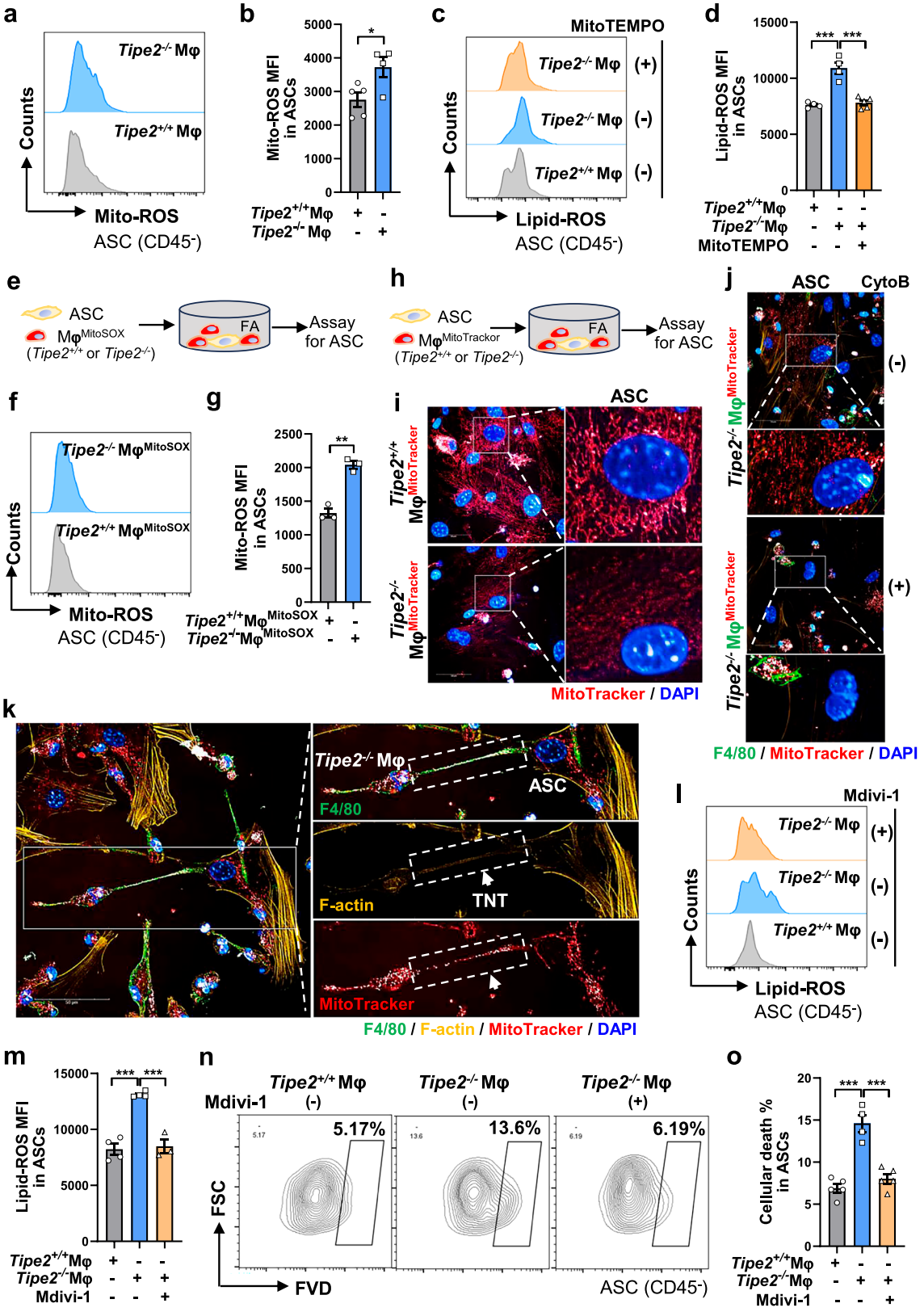

intercellular transportation of mitochondria between different cells[42–44]. To verify the contribution of TNT to mitochondrial transfer from *Tipe2*$^{-/-}$ macrophages to ASCs, we blocked TNT connection using cytochalasin B and found a sharp reduction in mitochondrial transportation (Fig. 5j). We further examined TNT structures in the coculture of ASCs and *Tipe2*$^{-/-}$ macrophages by staining F-actin with phalloidin. As expected, TNTs were clearly visible between ASCs and macrophages; and importantly, there was a perfect localization of macrophage-derived mitochondria (prelabelled with MitoTracker) within these TNTs (Fig. 5k). These observations support that intercellular TNTs are a major pathway for mitochondrial transfer from *Tipe2*$^{-/-}$ macrophages into ASCs. As fragmented mitochondria with

Fig. 5 | TIPE2-deficient macrophages drive ASC ferroptosis by propagating mitochondria fragmentation via TNTs. a, b Flow cytometry frequency (**a**) of mitochondrial ROS in ASCs with MFI quantification (**b**; $n = 4$ or 5) after 24 h coculture with *Tipe2*$^{+/+}$ or *Tipe2*$^{-/-}$ macrophages. **c, d** Flow cytometry frequency (**c**) of lipid ROS in ASCs with MFI quantification (**d**; $n = 4$ or 5) after 24 h coculture with *Tipe2*$^{+/+}$ or *Tipe2*$^{-/-}$ macrophages with or without 20 μM MitoTEMPO. **e-g**, Schematic diagram of coculture assay (**e**) for ASCs (wild-type) and MitoSOX-labeled macrophages (*Tipe2*$^{+/+}$ or *Tipe2*$^{-/-}$) in the presence of FA, and flow cytometry frequency (**f**) of macrophage-derived mitochondrial ROS in ASCs with MFI quantification (**g**; $n = 3$) after 24 h coculture. **h–j** Schematic diagram of coculture assay (**h**) for ASCs (wild-type) and MitoTracker-labeled macrophages (*Tipe2*$^{+/+}$ or *Tipe2*$^{-/-}$) in the presence of FA, and representative confocal imaging of macrophage-derived mitochondria in ASCs after 24 h coculture (**i**), or in the presence 350 nM cytochalasin B (CytoB) (**j**). Scale bars, 50 μm. **k** Representative confocal imaging of TNTs (F-actin, yellow) between ASCs and *Tipe2*$^{-/-}$ macrophages (F4/80, green) in the above coculture system and their co-localization with macrophage-derived mitochondria (red, MitoTracker). Nuclei (blue, DAPI). Scale bars, 50 μm. **l–o** Flow cytometry frequencies of lipid ROS with MFI quantification (**l, m**; $n = 3$ or 4) and cellular death (**n, o**; $n = 4$ or 5) in ASCs after 24 h coculture with *Tipe2*$^{+/+}$ or *Tipe2*$^{-/-}$ macrophages in presence or absence of 50 μM Mdivi-1. Data are presented as mean ± s.e.m. $^{*}P < 0.05$, $^{**}P < 0.01$, $^{***}P < 0.001$ determined by two-tailed student's *t*-test (b,g) or one-way ANOVA (d,m,o). Data are representative of at least two independent experiments.

abundant ROS were transferred from *Tipe2*$^{-/-}$ macrophages into ASCs, we then wondered the contribution of mitochondrial fragmentation on ASC death. Excitingly, in coculture with *Tipe2*$^{-/-}$ macrophages, blockade mitochondrial fission with Mdivi-1 significantly eliminated lipid ROS in ASCs whilst reducing ASC death (Fig. 5l–o). Collectively, these results indicate that TIPE2 deficiency in macrophages may cause a propagation of mitochondrial fragmentation toward ASCs, thereby contributing to ASC death by overloading mitochondrial ROS.

Tipe2$^{-/-}$ macrophage transfer promotes ASC ferroptosis and metabolic disorders in HFD-fed mice

To further verify the contribution of *Tipe2*$^{-/-}$ macrophages to ASC ferroptosis in vivo, we delivered MitoTracker-labeled *Tipe2*$^{-/-}$ macrophages into HFD-fed wild-type mice and found a successful settlement of macrophage-derived mitochondria into ASCs of VAT (Fig. 6a), thus confirming in vivo mitochondrial transfer from *Tipe2*$^{-/-}$ macrophages to ASCs. Based on this, HFD-fed wild-type mice were transferred with FA-pretreated *Tipe2*$^{-/-}$ or *Tipe2*$^{+/+}$ macrophages during the last 4 weeks of diet intervention. Relative to *Tipe2*$^{+/+}$ macrophages, *Tipe2*$^{-/-}$ macrophage transfer caused an increasing but statistically non-significant trend of body weight gain (Fig. 6b). Notably, *Tipe2*$^{-/-}$ macrophage transfer aggravated glucose intolerance and insulin resistance in HFD-fed mice, as manifested by increased levels of blood glucose post glucose or insulin injection compared to *Tipe2*$^{+/+}$ macrophage transfer (Fig. 6c–f). Of note, different from *Tipe2*$^{+/+}$ macrophages, *Tipe2*$^{-/-}$ macrophages dysregulated fat storage in VAT and liver tissue, with decreased ratios of VAT mass to body weight but increased ratio of liver weight to body weight (Fig. 6g, h). In line with this, *Tipe2*$^{-/-}$ macrophage transfer significantly increased 4-HNE in ASCs and reduced ASC pool in VAT, accompanied by increases in cellular death and mitochondrial ROS in ASCs (Fig. 6i–n). As such, adoptive transfer of *Tipe2*$^{-/-}$ macrophages could promote ASC ferroptosis in VAT and therefore accelerate metabolic disorders in HFD-fed mice.

TIPE2 restoration in VAT macrophages reduces ASC ferroptosis and metabolic disorders in HFD-fed mice

Next, we asked if TIPE2 restoration in VAT macrophages could correct ASC ferroptosis and VAT dysfunction in obese M-*Tipe2*$^{-/-}$ mice. Through *in site* administration with M-TIPE2 (recombinant AAV expressing macrophage-specific TIPE2) into HFD-fed M-*Tipe2*$^{-/-}$ mice, we showed that M-TIPE2 significantly retarded the increase of body weight gain independent on food intake (Fig. 7a and Supplementary Fig. 11a, b). Accordingly, TIPE2 restoration in VAT macrophages brought an improvement in glucose tolerance and insulin action in these mice, as suggested by decreases in the levels of blood glucose post glucose or insulin injection and corresponding area under the curve (Fig. 7b–e). More excitingly, M-TIPE2 treatment restored VAT expansion accompanied by a rebalance of VAT mass and liver weight, while inguinal SAT mass showed no obvious alteration (Fig. 7f, g and Supplementary Fig. 11c, d). In agreement with these changes, TIPE2 restoration in VAT macrophages obviously reduced aberrant adipocyte hypertrophy and downregulated 4-HNE in ASCs of HFD-fed M-*Tipe2*$^{-/-}$ mice (Fig. 7h, i and Supplementary Fig. 11e, f). Of note, ASC pool was remarkably reversed in VAT by M-TIPE2 treatment, accompanied by reductions in mitochondrial ROS and cellular death in ASCs (Fig. 7j–m). These data demonstrate that reconstruction of macrophage TIPE2 in VAT could partially correct metabolic disorders by reducing ASC ferroptosis to restore healthy VAT expansion. Of note, with the development of obesity, *Tipe2*$^{-/-}$ macrophages could continuously accumulate into VAT and thus substitute macrophages carrying exogenous TIPE2, thereby weakening their metabolic benefits.

TIPE2 deficiency induces mitochondrial fission by potentiating IP3R-Ca^{2+}-Drp1 axis in macrophages

Considering that *Tipe2*$^{-/-}$ macrophages could drive ASC ferroptosis by propagating mitochondrial fragmentation, we further explored the mitochondrial states in these macrophages. TIPE2 deficiency significantly upregulated mitochondrial ROS while downregulated mitochondrial membrane potential in macrophages (Supplementary Fig. 12a, b). Notably, *Tipe2*$^{-/-}$ macrophages had obviously smaller and shorter mitochondria than *Tipe2*$^{+/+}$ macrophages as determined by transmission electron microscopy (Fig. 8a), supporting that TIPE2 deficiency caused mitochondrial fragmentation in these macrophages and therefore upregulated mitochondrial ROS. Mitochondria undergo fission and fusion in response to metabolic demands or stresses. Disbalance of mitochondrial dynamics, such as excessive fission, impaired fusion or disabled mitochondrial autophagy, may contribute to mitochondrial fragmentation in the cells. Dynamin-related protein 1 (Drp1) is the key GTP enzyme that initiates mitochondrial fission. Upon dephosphorylation at Ser637 by calcium (Ca^{2+}) -dependent calcineurin, Drp1 can translocate onto the outer membrane of mitochondria to form the contraction loop[45–47]. We then asked whether TIPE2 deficiency affected the process of mitochondrial fission in macrophages. In agreement with data from transmission electron microscopy, MitoTracker staining confirmed smaller and shorter mitochondria in *Tipe2*$^{-/-}$ macrophages rather than in *Tipe2*$^{+/+}$ macrophages; importantly, TIPE2 deficiency caused an upregulation of Drp1 protein, which colocalized with mitochondria in these macrophages (Fig. 8b). This indicates that TIPE2 deficiency may induce Drp1 activation and its translocation onto mitochondria, an initial step dictating mitochondrial fission. Exactly, upon treatment with Mdivi-1, mitochondrial fragmentation caused by TIPE2 deficiency was remarkably inhibited (Fig. 8c; Supplementary Fig. 12c), suggesting that TIPE2 deficiency induces mitochondrial fission in macrophages through activating Drp1. In line with these observations, FA treatment caused obvious TIPE2 reduction, accompanied by smaller and shorter mitochondria in RAW264.7 macrophages; while TIPE2 overexpression successfully reversed this mitochondrial fragmentation (Supplementary Fig. 12d, e). And Drp1 protein was significantly reduced by TIPE2 overexpression in both cytoplasm and mitochondria (Supplementary Fig. 12f). These findings demonstrate that TIPE2 is a key checkpoint for Drp1-mediated mitochondrial fission and thereby determines mitochondrial homeostasis in macrophages.

https://doi.org/10.1038/s41467-025-62690-1

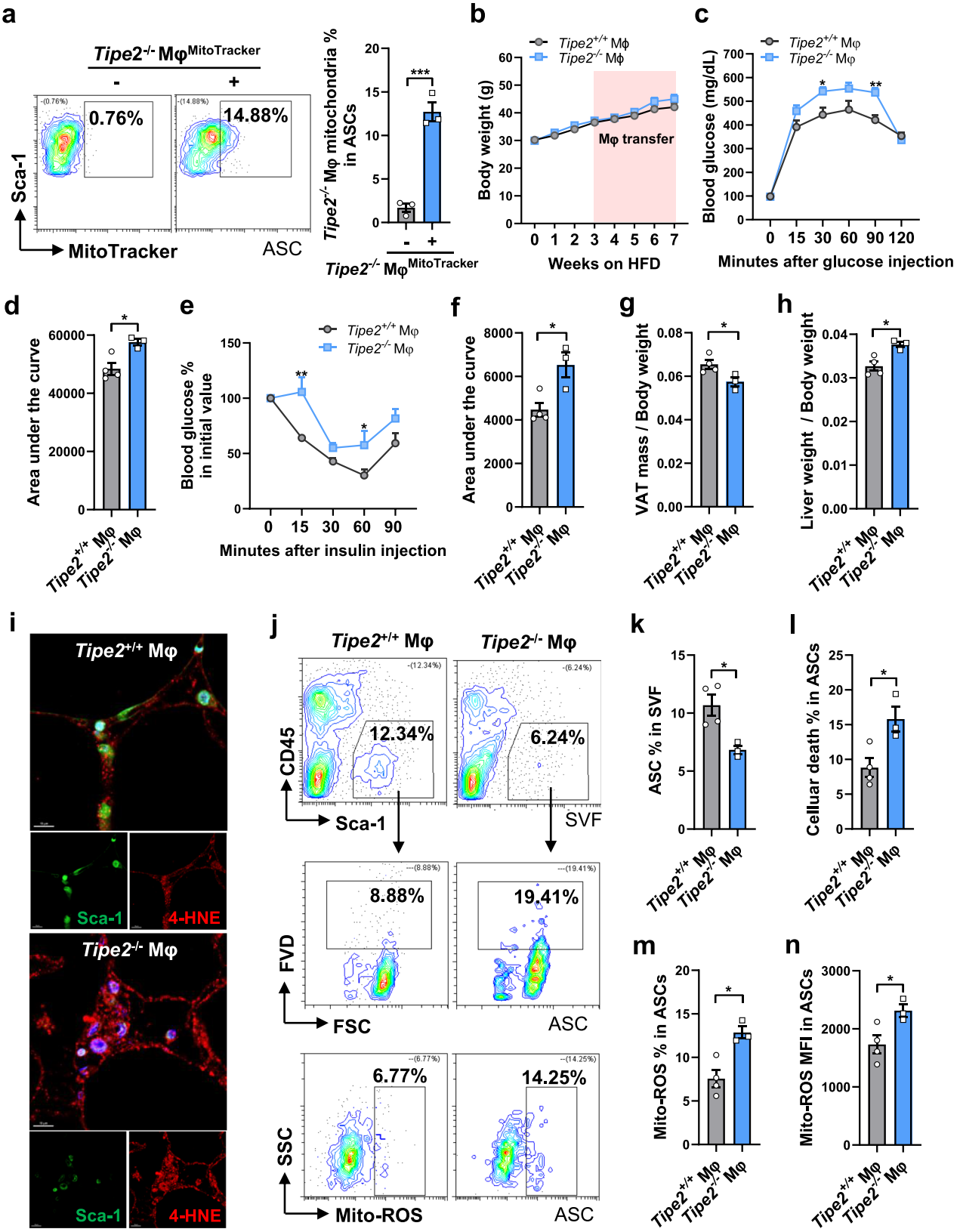

Fig. 6 | *Tipe2*$^{-/-}$ macrophage transfer promotes ASC ferroptosis and metabolic disorders in HFD-fed mice. a Flow cytometry frequency of *Tipe2*$^{-/-}$ macrophage-derived mitochondria in ASCs of SVF from HFD-fed wild-type mice received intraperitoneal transfer of *Tipe2*$^{-/-}$ macrophages (labeled with MitoTracker and treated with FA for 18 h). $n = 3$ mice per group. **b**–**f** Body weight change (**b**), glucose tolerance test with area under the curve (**c, d**), insulin tolerance test with area under the curve (**e, f**) in mice received intraperitoneal transfer of *Tipe2*$^{+/+}$ or *Tipe2*$^{-/-}$ macrophages (18 h pretreatment with FA) during the last 4 weeks of HFD feeding (7 weeks). 2×10^6 macrophages per mice, every 3 days. **g, h** Ratios of EpiVAT mass (**g**), liver weight (**h**) to body weight. **i**, Representative confocal imaging of immunofluorescence for 4-HNE (red) in ASCs (Sca-1, green) in VAT sections. Scale bars, 10 μm. **j**–**n** Flow cytometry frequencies of ASCs in SVF (**j, k**), cellular death in ASCs (**j, l**), mitochondrial ROS in ASCs (**j,m**) with MFI quantification (**n**) in VAT. $n = 5$ mice per group (b), $n = 3$ or 4 mice per group (c-h, k-n). Data are presented as mean ± s.e.m. $^*P < 0.05$, $^{**}P < 0.01$, $^{***}P < 0.001$ determined by two-tailed student's *t*-test (**a, d, f–h, k–n**) or two-way ANOVA (c,e).

To clarify how TIPE2 affected Drp1 activity, we next examined cytoplasmic Ca^{2+} in *Tipe2*$^{-/-}$ macrophages, which determines calcineurin activity and subsequent Drp1 activation. TIPE2 deficiency caused an elevation in cytoplasmic Ca^{2+} in macrophages as determined by Fluo-4 AM (Fig. 8d). Interestingly, the inositol 1,4,5-trisphosphate receptor (IP3R), a Ca^{2+}-release channel mainly located in endoplasmic reticulum, was markedly upregulated by TIPE2 deficiency, together with Drp1 dephosphorylation at Ser637 and upregulation in these macrophages (Fig. 8e). To connect the aberrant IP3R-Ca^{2+} signaling to Drp1 activity in these cells, we treated *Tipe2*$^{-/-}$ macrophages with Ca^{2+} chelator BAPTA, followed by examination of Drp1-mediated mitochondrial fragmentation. As a result, BAPTA caused an increase in Drp1 phosphorylation at Ser637 and a decrease in Drp1 protein, and thus reduced mitochondrial fragmentation and mitochondrial ROS in these macrophages (Fig. 8f, g and Supplementary Fig. 12g, h). Furthermore, the IP3R antagonist 2-APB successfully abolished the elevation of intracellular Ca^{2+} caused by TIPE2 deficiency, thereby preventing excessive mitochondrial fission and fragmentation in these macrophages (Fig. 8h and Supplementary Fig. 12i, j). This process coincided with an increase in Drp1 phosphorylation at Ser637 while a decrease in Drp1 protein (Fig. 8i), eventually reducing mitochondrial ROS in these macrophages (Supplementary Fig. 12k). In addition, phosphatidylinositol 4,5-bisphosphate (PIP2), the precursor for IP3 production, showed a marked increase in *Tipe2*$^{-/-}$ macrophages compared with *Tipe2*$^{+/+}$ macrophages, particularly on their plasma membrane (Supplementary Fig. 12l), plausibly explaining IP3R upregulation caused by TIPE2 deficiency. Interestingly, immunofluorescence showed an apparent colocalization of TIPE2 with IP3R in wild-type macrophages (Fig. 8j). Antibodies against TIPE2 or IP3R successfully immunoprecipitated both TIPE2 and IP3R in the lysates of these macrophages, suggesting that TIPE2 interacts with IP3R in wild-type macrophages (Fig. 8k). Previous studies demonstrate that actin-associated IP3R clusters beneath plasma membrane act as the license that allows the Ca^{2+} puffs and global cytosolic Ca^{2+} signaling[48]. We next examined IP3R and actin filaments in *Tipe2*$^{-/-}$ macrophages. Consistently, there were apparent IP3R clusters alongside F-actin assembly in *Tipe2*$^{-/-}$ macrophages rather than *Tipe2*$^{+/+}$ macrophages (Fig. 8l), supporting that TIPE2 may serve as a valve to control IP3R clustering and consequent rise of intracellular Ca^{2+}. Collectively, TIPE2 is a pivotal controller of mitochondrial fission and fragmentation in macrophages by controlling IP3R-Ca^{2+}-Drp1 axis.

Discussion

In response to persistent overnutrition, visceral fat undergoes progressive dysfunction, accompanied by dramatic changes in macrophages and ASCs, such as M1 polarization and ASC senescence[17,20]. Here, we defined ASC ferroptosis beyond senescence in pathological mouse VAT, providing further explanation for ASC exhaustion in morbid obesity. Meanwhile, we identified the distinct phenotype of TIPE2 loss in VAT macrophages upon obesity. Based on several lines of in vivo evidence, we established a causal link of TIPE2 loss in macrophages to ASC ferroptosis during VAT dysfunction and metabolic disorders. Firstly, spatial proximity of macrophages to ASCs provided a scaffold for their possible cross-talk in VAT under high-fat condition. Secondly, TIPE2 deficiency in macrophages aggravated HFD-induced obesity and metabolic abnormities by promoting ASC ferroptosis and exhaustion, which impaired adipogenesis to disturb fat storage by VAT and therefore promote severe fatty liver. Lastly, *Tipe2*$^{-/-}$ macrophage transfer accelerated ASC ferroptosis and VAT maladaptation to metabolic stress in wild-type mice in the early phase of HFD feeding; while TIPE2 restoration in VAT macrophages ameliorated ASC ferroptosis and metabolic dysfunction in obese M-*Tipe2*$^{-/-}$ mice. It is evident that a high-fat microenvironment may reduce TIPE2 protein in VAT macrophages, which further promotes ASC ferroptosis to elicit a detrimental metabolic outcome. Besides fatty acids, inflammatory stimuli like LPS can induce TIPE2 downregulation in macrophages[22,33]. As these inflammatory factors often increase with HFD-associated obesity, it is reasonable that they may collaborate with fatty acids to reduce TIPE2 in WAT macrophages. In line with this, TIPE2 overexpression in VAT macrophages effectively ameliorated HFD-induced obesity and metabolic dysfunction in wild-type mice (Supplementary Fig. 13a–d), probably by counteracting the above insults in the high-fat microenvironment. Interestingly, even without high-fat challenge, TIPE2 loss in macrophages could cause mild adipocyte hypertrophy and an increasing trend of ASC death in VAT (Fig. 3b; Supplementary Fig. 6f, g), together with moderate increase in hepatic triglyceride (Fig. 2j). In either insulin sensitive or resistant state, substrate delivery including fatty acid flux from WAT is a large contributor to hepatic triglyceride independent of insulin[49–51]. In this case, it is plausible that NCD-fed M-*Tipe2*$^{-/-}$ mice could direct excess fatty acids from WAT toward the liver to increase hepatic triglyceride. This process probably resulted from hypertrophic adipocytes with increased lipolysis or reduced lipid uptake[50,52], and therefore, caused a compensatory regulation by hepatic triglycerides. Nonetheless, other intrahepatic regulatory mechanisms likely involved remain to be further determined. Collectively, these findings reveal a previously unrecognized role of obesity-associated VAT macrophages in disturbing ASC-based metabolism beyond mediating inflammation. Besides, our study generated M-*Tipe2*$^{-/-}$ mice by crossing *Tipe2*$^{fl/fl}$ mice with *LysMCre* mice, which are commonly used in *Cre-lox* studies for myeloid cell lineage, including adipose tissue macrophages[53,54]. Since most myeloid cells in adipose tissue are macrophages rather than granulocytes, it is plausible that the primary effects caused by M-*Tipe2*$^{-/-}$ mice could be attributed to TIPE2-deficient macrophages. Furthermore, metabolic improvement by TIPE2 restoration in VAT macrophages could also support the roles of TIPE2-deficient macrophages in these M-*Tipe2*$^{-/-}$ mice. Despite this, we cannot exclude possible effects from other TIPE2-deficient myeloid cells yet, such as neutrophils involved in early phase of adipose tissue inflammation in obesity. This will be an interesting area deserving further investigation.

Through cell-cell contact coculture, we demonstrated the direct effects of *Tipe2*$^{-/-}$ macrophages on ASC ferroptosis. TIPE2 deficiency caused a propagation of mitochondrial fragmentation from macrophages to ASCs, thereby promoting their ferroptosis due to mitochondrial ROS overload. Accumulating studies have reported mitochondrial transfer from mesenchymal stem cells into recipient cells, including macrophages, thus providing healthy mitochondria to improve the functions of recipient cells or rescue them from injuries[42,55,56]. More interestingly, tissue-resident macrophages can remove damaged mitochondria from stressed adipocytes to facilitate intra- or inter-organ homeostasis of brown adipose tissue and heart[57,58]. In this study, we unexpectedly revealed an opposite direction of mitochondrial transfer from macrophages into ASCs, which was driven by loss of macrophage TIPE2, a kind of stressed phenotype in high-fat conditions. This transportation imposed fragmented mitochondria with high ROS on ASCs and thus increased their susceptibility to ferroptosis. Of note, there were evident intercellular TNTs between these macrophages and ASCs in FA-rich circumstances, indicating that TNTs serve as the crucial hubs in charge of transporting these mitochondria. In this regard, TNT-based propagation of mitochondria fragmentation from TIPE2-ablated macrophages may act as a culprit of ASC ferroptosis. Interestingly, extracellular vesicles have also been identified as an important pathway to deliver mitochondrial components into target cells[42,59–61]. In fact, exosomes from both *Tipe2*$^{+/+}$ and *Tipe2*$^{-/-}$ macrophages also contained mitochondrial protein TOMM20 (Supplementary Fig. 14a). As shown in mitochondria tracking assay, ASCs could obtain mitochondrial parts from supernatants of *Tipe2*$^{+/+}$ or *Tipe2*$^{-/-}$ macrophages (prelabelled with MitoTracker), which were partially inhibited by exosome inhibition (Supplementary Fig. 14b). Thus, mitochondrial transfer via

https://doi.org/10.1038/s41467-025-62690-1

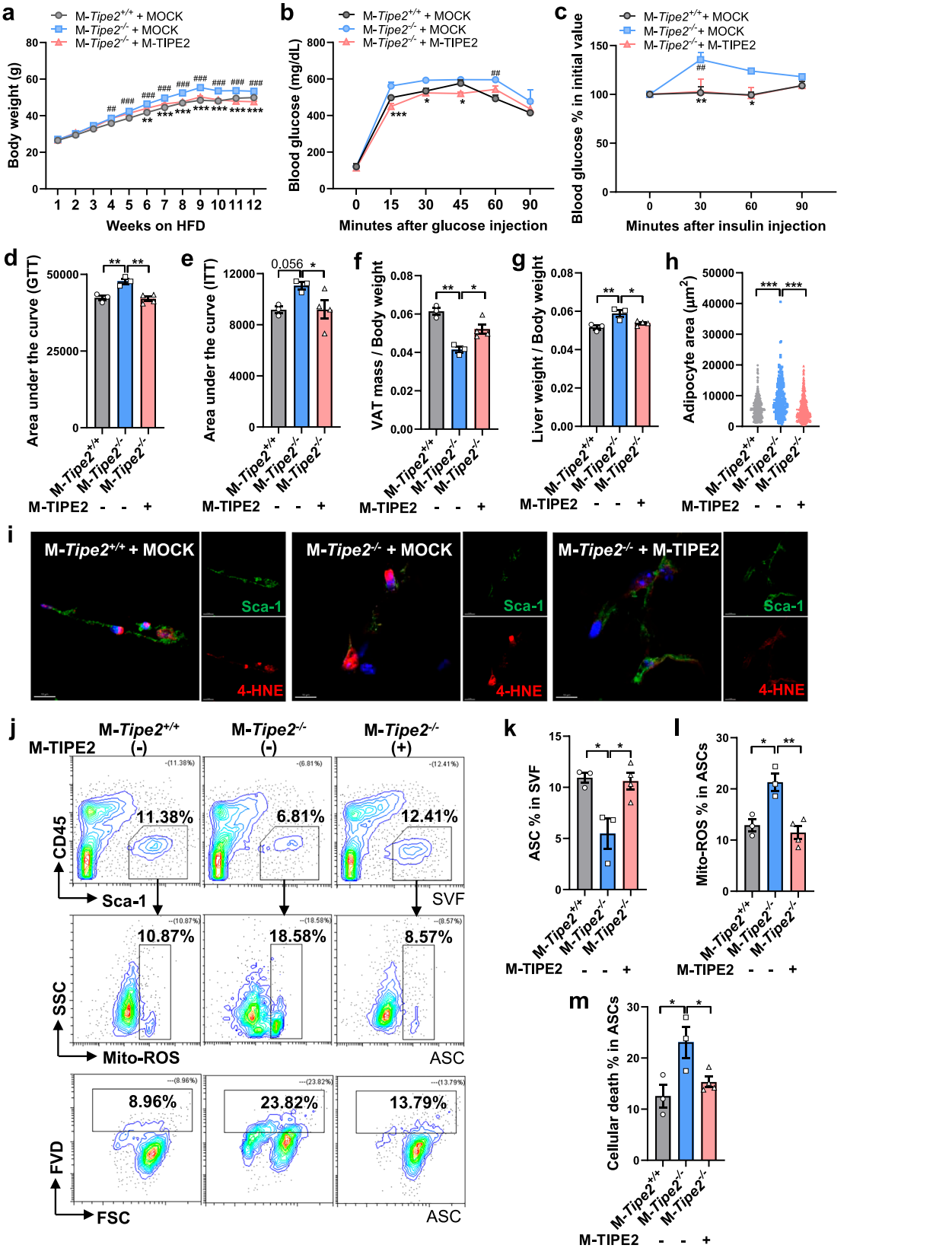

Fig. 7 | TIPE2 restoration in VAT macrophages reduces ASC ferroptosis and metabolic disorders in HFD-fed M-*Tipe2*$^{-/-}$ mice. a–e Body weight change (**a**), glucose tolerance test (**b**) and insulin tolerance test (**c**) with corresponding area under the curve (**d, e**) in M-*Tipe2*$^{+/+}$ and M-*Tipe2*$^{-/-}$ mice received M-TIPE2 (recombinant AAV expressing EGFP-fused TIPE2 in F4/80^{+} macrophages) in visceral fat 2 weeks after HFD intervention (12 weeks). **f, g** Ratios of EpiVAT mass (**f**), liver weight (**g**) to body weight. **h** Statistical analysis of adipocyte sizes in VAT sections ($n \geq 262$ adipocytes examined over 3 mice per group). **i** Representative confocal imaging of immunofluorescence for 4-HNE (red) in ASCs (Sca-1, green) in VAT sections. Scale bars, 10 μm. **j–m** Flow cytometry frequencies of ASCs in SVF (**j, k**), mitochondrial ROS in ASCs (**j, l**), cellular death in ASCs (**j, m**) in VAT of the mice. $n = 3$ or 4 mice per group (**a–g**; **k–m**). Data are presented as mean ± s.e.m. #$P < 0.05$, ##$P < 0.01$, ###$P < 0.001$ (M-*Tipe2*$^{+/+}$+MOCK vs. M-*Tipe2*$^{-/-}$+MOCK in **a–c**); *$P < 0.05$, **$P < 0.01$, ***$P < 0.001$ (M-*Tipe2*$^{-/-}$+MOCK vs. M-*Tipe2*$^{-/-}$+M-TIPE2 in **a–c**) determined by two-way (**a–c**) or one-way ANOVA (**d–h**,**k–m**).

extracellular vesicles of macrophages could be another contributor to the mitochondrial state of ASCs. And it is valuable to carefully discern the complex package of extracellular vesicles from macrophages, such as healthy, damaged, oxidative mitochondria, or various mitochondrial proteins, which may produce different effects in different microenvironments.

Aside from mitochondrial ROS overload, another culprit of ASC ferroptosis is Fe^{2+} overload caused by *Tipe2*$^{-/-}$ macrophages. Ferritin in mammals serves as an iron storage protein, confining ferric iron (Fe^{3+}) in nontoxic and bioavailable form. Its H-subunit FTH possesses a ferroxidase center to convert Fe^{2+} to Fe^{3+}, while L-subunit FTL facilitates iron core formation[41,62,63]. So, ferritin, especially FTH, plays a critical role in maintaining intracellular iron homeostasis. Previous studies have demonstrated that exosomal ferritin from human macrophages is required for maintaining serum ferritin[41,64]. Here, we demonstrated that in high-fat conditions, TIPE2-ablated macrophages reduced exosomal ferritin and failed to upregulate ferritin in ASCs, therefore increasing the susceptibility of ASCs to ferroptosis via an overload of intracellular Fe^{2+}. Of note, ferritin decrease in exosomes might be attributed to its downregulation in source macrophages that was caused by TIPE2 deficiency. A possible explanation for TIPE2 deficiency-elicited ferritin decline in macrophages could be ferritinophagy[65,66], largely due to TIPE2 regulation in autophagy flux or mTORC1 activity[23,24,27], which remains an open area to be explored.

In terms of mitochondrial fragmentation caused by TIPE2 deficiency, our data defined an aberrant IP3R-Ca^{2+}-Drp1 axis in driving excessive mitochondrial fission, evidenced by multiple blockade assays in *Tipe2*$^{-/-}$ macrophages. Firstly, TIPE2 deficiency caused mitochondrial fragmentation together with Drp1 dephosphorylation (Ser637) and Drp1 accumulation in mitochondria, while Mdivi-1 abrogated Drp1 activation to prevent mitochondrial fragmentation in these cells. This confirms that TIPE2 deficiency could induce Drp1-mediated mitochondrial fission in macrophages. Secondly, TIPE2 deficiency led to an upregulation of IP3R together with a surge of cytoplasmatic Ca^{2+}; while blockade of IP3R or cytoplasmic Ca^{2+} successfully inhibited Drp1 activation and mitochondrial fission, supporting the essential role of IP3R-mediated Ca^{2+} release in this process. These findings demonstrate that TIPE2 loss is the primary cause for the aberrant IP3R-Ca^{2+}-Drp1 axis and excessive mitochondrial fission in macrophages. It has been recognized that TIPE family proteins have a homologous TH domain that can bind to phosphoinositides, including PIP2[34]. In line with this, TIPE2 deficiency led to an increase of PIP2 in macrophages, particularly on the plasma membrane. As membrane PIP2 determines the production of IP3 catalyzed by phospholipase C (PLC)-γ, it is plausible that TIPE2 deficiency entails more membrane PIP2 available for PLC-γ and thus more IP3 production to activate IP3R. Notably, IP3R is identified as an inhibitory target of TIPE2 in macrophages. TIPE2 deficiency may release IP3R to allow its clustering on actin assembly, whilst the latter can be initiated by the elevation of PIP2. This process may promote Ca^{2+} rise to induce Drp1 activation and subsequent mitochondrial fission. Thus, TIPE2 is indispensable to constrain the aberrant IP3R-Ca^{2+}-Drp1 axis, whereby Drp1-mediated mitochondrial fission and fragmentation were precisely controlled in macrophages. Upon TIPE2 loss, the aberrant IP3R-Ca^{2+}-Drp1 axis may trigger excessive mitochondrial fission in macrophages, and these fragmented mitochondria propagate from macrophages to ASCs, causing mitochondrial ROS overload to promote ASC ferroptosis.

It should be noted that, in spite of mitochondrial fission and ROS increment, *Tipe2*$^{-/-}$ macrophages, relative to *Tipe2*$^{+/+}$ macrophages, showed no significant alteration in cellular death, similar to that in ASC coculture system (Supplementary Fig. 15a, b). And there was no significant difference in the death of $CD45^+$ immune cells in VAT between HFD-fed M-*Tipe2*$^{-/-}$ and M-*Tipe2*$^{+/+}$ mice (Supplementary Fig. 15c). These observations implied that TIPE2 deficiency did not increase the risk of ferroptosis in macrophages. One plausible explanation for this ferroptosis resistance could be mTORC1 activation caused by TIPE2 deficiency and consequent GPX4 protein increment, both of which could be abrogated by rapamycin (Supplementary Fig. 15d, e). In support of these findings, previous studies have documented the inhibitory effect of TIPE2 on mTORC1 activation and the promotive effect of mTORC1 on GPX4 protein expression[23,24,67]. Besides, we unexpectedly found a decrease of Fe^{2+} in *Tipe2*$^{-/-}$ macrophages relative to *Tipe2*$^{+/+}$ macrophages (Supplementary Fig. 15f), which could be another contributor to ferroptosis resistance and a reasonable trigger of ferritin decline in *Tipe2*$^{-/-}$ macrophages.

Taken together, we reveal a previously unrecognized intercellular cross-talk between macrophages and ASCs during VAT maladaptation to obesity. Macrophages with a distinct phenotype of TIPE2 loss dictate ASC ferroptosis, thereby disrupting adaptive VAT expansion to promote series of metabolic abnormalities. We identify two critical pathways in dictating ASC ferroptosis by TIPE2-ablated macrophages: TNT-based propagation of mitochondrial fragmentation and exosome-mediated dysregulation of ferritin transportation from macrophages into ASCs, jointly contributing to ASC ferroptosis by overload of mitochondrial ROS and intracellular Fe^{2+}. We also unravel a regulatory mechanism by which TIPE2 controls excessive mitochondrial fission through IP3R-Ca^{2+}-Drp1 axis in macrophages (Supplementary Fig. 16). These findings propose opportunities for correcting obesity-associated ASC ferroptosis and visceral fat dysfunction by targeting TIPE2 loss and related mitochondrial fragmentation in VAT macrophages, which benefits the treatment of obesity and metabolic disorders. Nonetheless, some open and interesting areas remain to be explored. For instance, possible regulation of TIPE2 on other cell types such as adipocytes, probably in some special subsets or some distinct obesity-associated pathologies, is yet to be determined. As HFD feeding could also induce mitochondrial fragmentation in white adipocytes[68], it remains to be uncovered whether other cell types including adipocytes could receive or suffer from macrophage-derived mitochondrial fragmentation. In addition, the regulation of macrophage ferritin is another prospective field for potential clinical importance. But different from the detrimental effects of TIPE2-deficient macrophages, macrophage-specific FTH1 knockout, which altered gene expression related to iron metabolism, unexpectedly alleviated obesity and associated metabolic dysfunction by inhibiting macrophage inflammation[69]. As such, more careful investigations are required to elucidate the mechanisms by which TIPE2 deficiency causes ferritin reduction in macrophages. This may result from a secondary reaction to mitochondrial fragmentation or an incapability to handle the iron cycle. Moreover, in terms of Ferrostatin-1 treatment, it is evident that ferroptosis inhibition could successfully rescue VAT ASCs in HFD state. Given the key role of WAT in regulating systemic insulin action, it is reasonable to attribute systemic metabolic improvement to the reduction of ASC ferroptosis, at least partially by Ferrostatin-1 treatment. Nonetheless, we cannot exclude the contribution of ferroptosis inhibition in other tissues, such as the liver. This is another area deserving further exploration, in which cell types of ferroptosis and possible metabolic outcome in obesity should be considered. For instance, hepatocytes may function in both glycogenesis and gluconeogenesis, which differentially regulate glucose metabolism in insulin-sensitive or resistant state and are heavily affected by WAT function[51]. In this context, either induction or inhibition of ferroptosis may produce multiple and complicated effects on blood glucose regulation, which require careful evaluation.

Methods

Animals

All of the animal studies were in accordance with the institutional guidelines and relevant ethical regulations for animal care and utilization, and approved by the Ethical Committee of the School of Basic Medical Sciences, Shandong University. Male mice were used in this study. C57BL/6J mice were obtained from Vital River Laboratory

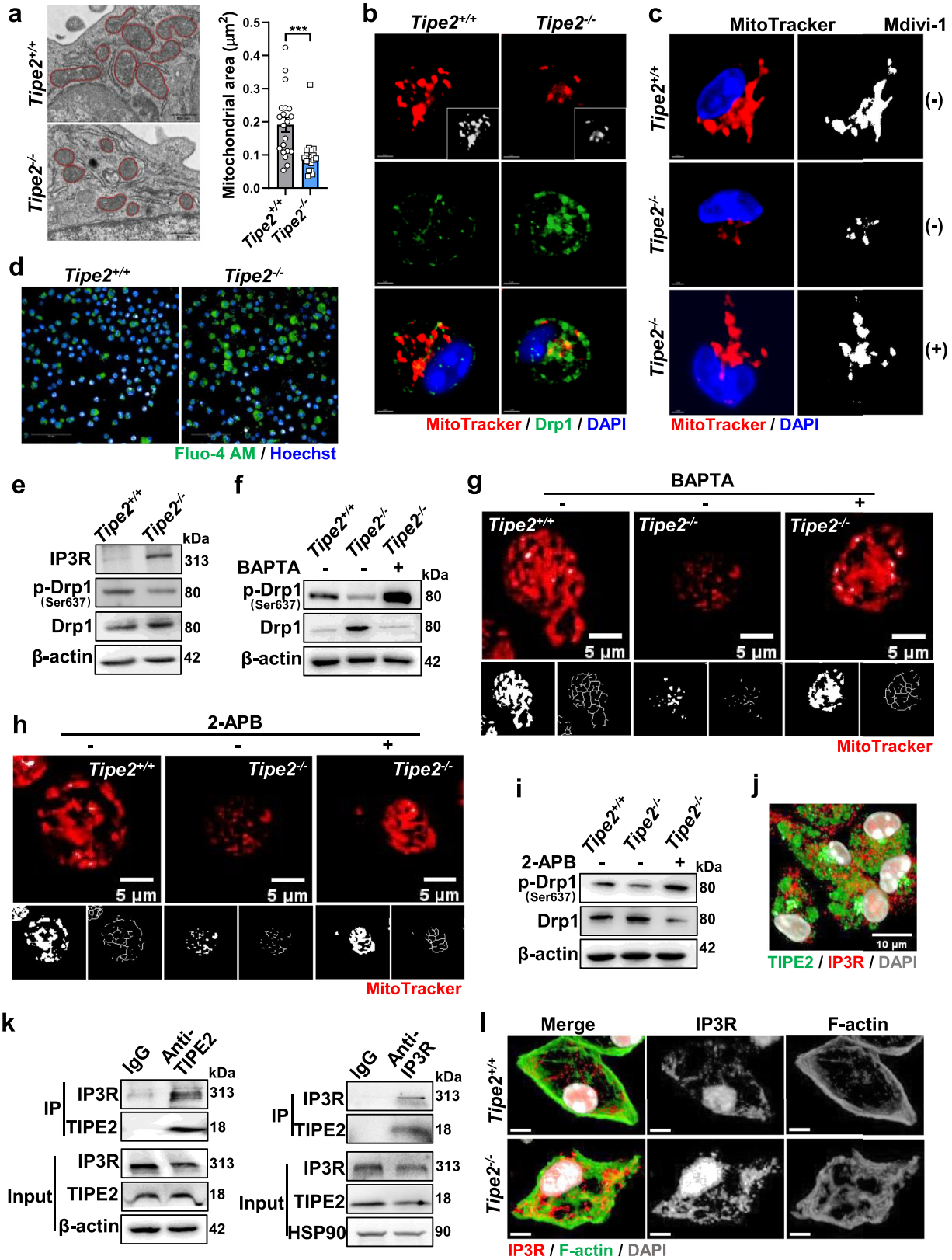

Animal Technology (Beijing, China). *Tipe2* knockout (*Tipe2*$^{-/-}$) mice and *Tipe2*$^{flox/flox}$ (*Tipe2*$^{fl/fl}$; two *loxP* sites flanking *Tipe2* exon 2) mice were created on C57BL/6J background using CRISPR-Cas9 technique (Biocytogen Pharmaceutical, Beijing, China). Myeloid cell-specific *Tipe2* knockout (M-*Tipe2*$^{-/-}$) mice were generated by crossing *Tipe2*$^{fl/fl}$ mice with *LysMCre* mice (The Jackson Laboratory) carrying Cre recombinase in lysozyme 2 gene locus. Mice were maintained on a 12:12 h light/dark cycle at 22 °C ± 2 °C in the Model Animal Research Center.

Cell culture

Primary *Tipe2*$^{+/+}$ or *Tipe2*$^{-/-}$ macrophages were harvested from peritoneal lavage fluid in starch-induced mice at 6–8 weeks of age. After 4 h of attachment, the cells were cultured in complete DMEM containing

Fig. 8 | TIPE2 deficiency induces mitochondrial fission by potentiating IP3R-Ca^{2+}-Drp1 axis in macrophages. a Representative transmission electron microscopy images for mitochondrial morphology and statistical analysis of mitochondrial area ($n \geq 20$) in *Tipe2*$^{+/+}$ or *Tipe2*$^{-/-}$ macrophages. Scale bars, 500 nm. **b** Representative confocal imaging of immunofluorescence for mitochondria (MitoTracker, red; inset, grayscale images) and Drp-1 (green) in *Tipe2*$^{+/+}$ or *Tipe2*$^{-/-}$ macrophages. Nuclei (DAPI, blue). Scale bars, 3 μm. **c** Representative confocal imaging of mitochondria (MitoTracker, red; right, binary images) in *Tipe2*$^{+/+}$ or *Tipe2*$^{-/-}$ macrophages after 18 h treatment with or without 50 μM Mdivi-1. Nuclei (DAPI, blue). Scale bars, 2 μm. **d** Representative confocal imaging of intracellular Ca^{2+} (Fluo-4 AM, green) in *Tipe2*$^{+/+}$ or *Tipe2*$^{-/-}$ macrophages. Scale bars, 50 μm. **e, f** Representative immunoblots for indicated proteins in *Tipe2*$^{+/+}$ or *Tipe2*$^{-/-}$ macrophages (**e**), or post 2 h treatment with or without 10 μM BAPTA (**f**). **g,h** Representative confocal imaging of mitochondria (MitoTracker, red; bottom, binary images and skeletonized branches) in *Tipe2*$^{-/-}$ or *Tipe2*$^{+/+}$ macrophages after 2 h treatment with or without 10 μM BAPTA (**g**), 50 μM 2-APB (**h**), respectively. Scale bars, 5 μm. **i**, Immunoblots for indicated proteins in *Tipe2*$^{+/+}$ or *Tipe2*$^{-/-}$ macrophages post 2 h treatment with or without 50 μM 2-APB. **j** Representative confocal imaging of immunofluorescence for TIPE2 (green) and IP3R (red) in *Tipe2*$^{+/+}$ macrophages. Nuclei (DAPI, gray). Scale bars, 10 μm. **k** Representative blots for IP3R and TIPE2 proteins in *Tipe2*$^{+/+}$ macrophage lysates immunoprecipitated by antibodies against TIPE2 or IP3R. **l** Representative confocal imaging of immunofluorescence for F-actin (green) and IP3R (red) in *Tipe2*$^{+/+}$ or *Tipe2*$^{-/-}$ macrophages. Nuclei (DAPI, gray). Scale bars, 5 μm. Data are representative of at least two independent experiments. $^{***}P < 0.001$ determined by two-tailed student's *t*-test (**a**).

10% fetal bovine serum (FBS) plus 1% streptomycin/penicillin. ASCs were isolated from wild-type mice at 10–12 weeks of age as previously described[3,18]. Briefly, epididymal fat pads were digested in Krebs-Ringer Bicarbonate buffer supplemented with 2 mg/mL collagenase I (Worthington, Lakewood, NJ). After filtration through a 100 μm mesh, the SVF was collected, washed and cultured in complete DMEM. After 24 h, non-adherent cells were removed and the adherent ASCs were maintained in complete DMEM supplemented with 5 ng/mL basic fibroblast growth factor (Peprotech, Rocky Hill, NJ). The 3rd-4th passages of ASCs were used for the experiments.

Diet-induced obesity, adoptive cell transfer and AAV infection in mice

M-*Tipe2*$^{+/+}$, M-*Tipe2*$^{-/-}$ mice or wild-type mice at 8 weeks of age were fed a HFD (60% of total calories; Trophic Animal Feed High-tech, Nantong, China) to induce obesity, using mice fed a NCD as lean controls. For macrophage transfer, wild-type mice fed on HFD were intraperitoneally injected with *Tipe2*$^{+/+}$ or *Tipe2*$^{-/-}$ macrophages during the last 4 weeks of diet intervention. The macrophages were pretreated with FA (50 μM palmitic acid and 100 μM oleic acid; Sigma-Aldrich, St Louis, MO) for 18 h, and 2×10^6 cells per mice were used every 3 days. To restore TIPE2 expression in VAT macrophages, M-*Tipe2*$^{-/-}$ mice fed on HFD were injected with recombination adeno-associated virus (AAV; serotype 9) expressing EGFP-fused TIPE2 driven by F4/80 promoter (M-TIPE2; GeneChem, Shanghai, China) two weeks after diet intervention, using mice administered with AAV expressing EGFP as controls. Equal amounts of AAV (2×10^{11} genome copies per mouse) were injected into multiple sites of bilateral epididymal fat pads. Metabolic measurement and tissue collection were performed 7–10 weeks after AAV infection. In some condition, HFD-fed wild-type mice were used for AAV-mediated M-TIPE2 restoration in VAT. In other experiments, Ferrostatin-1 (Selleck, Houston, TX) was intraperitoneally injected into HFD-fed mice during the last 5 weeks of diet intervention (1 mg/kg body weight per mice per day), followed by metabolic measurement and tissue collection.

Metabolic parameter measurement

Glucose tolerance test was performed in mice with an overnight fast. The mice were intraperitoneally injected with D-glucose (2 g/kg body weight; Sigma-Aldrich), and the levels of blood glucose were measured at different time points. Insulin tolerance test was performed in mice with free access to food or fasted for 6 h. The mice were intraperitoneally injected with human insulin (0.75units/kg body weight; Wanbang, Xuzhou, China), and the levels of blood glucose were measured at different time points.

Hepatic lipid measurement

Hepatic lipids were extracted using Folch method. Briefly, liver tissue was homogenized in chloroform/methanol (2:1 v/v). The lipid-containing organic phase separated from the aqueous phase was collected and dried. The contents of triglyceride and total cholesterol were measured using commercial kits (Jiancheng Bio-engineering Institute, Nanjing, China) and normalized to tissue mass. In some conditions, neutral lipids were assayed in frozen sections of liver tissue using Oil Red O (Sigma-Aldrich) staining. Nuclei were stained with hematoxylin. And the sections were visualized by VS120 Virtual Slide Microscope (OLYMPUS, Tokyo, Japan).

Histology and lipofuscin autofluorescence detection

Mouse tissues fixed with 4% paraformaldehyde were embedded with paraffin and prepared into sections (Servicesbio, Wuhan, China). The sections were stained with hematoxylin and eosin (H&E) followed by visualization using VS120 Virtual Slide Microscope. Adipocyte sizes were evaluated in adipose tissue sections using ImageJ software. At least 10 randomly selected areas were included in 6 sections of 3 mice in each group. Lipofuscin was detected in paraffin-embedded adipose tissue sections based on its autofluorescence, referring to previous studies[30,70]. The combination of the following channels was used: channel 1, $\lambda_{ex}/\lambda_{em}$ = 488 nm/507 nm; channel 2, $\lambda_{ex}/\lambda_{em}$ = 561 nm/594 nm; channel 3, $\lambda_{ex}/\lambda_{em}$ = 637 nm/650 nm.

Coculture of macrophages and ASCs

Primary *Tipe2*$^{+/+}$ or *Tipe2*$^{-/-}$ macrophages (2.5×10^5 per well) were cocultured with ASCs (5×10^4 per well) via cell-cell contact in a 12-well plate. After 6 h of attachment, the cells were incubated with complement DMEM containing FA (50 μM palmitate acid and 100 μM oleic acid) in conjugation with bovine serum albumin (BSA, free of FA; Sigma-Aldrich) for another 24 h, using DMEM containing equal amounts of vehicle in conjugation with BSA as control. ASC ferroptosis was evaluated by lipid ROS and cell viability as mentioned below. In some condition, DFO (100 μM, APExBIO, Houston, TX), Ferrostatin-1 (5 μM, Selleck), z-VAD-FMK (20 μM, APExBIO), Necrostatin-1 (2 μM, APExBIO), Mdivi-1 (50 μM, MCE, Monmouth, NJ) or 20 μM Mito-TEMPO (Sigma-Aldrich) was added during coculture before assay for cell death. In other condition, ASCs were pretreated with RSL3 (250 nM, APExBIO) for 6 h before the coculture.

Exosome isolation from macrophages

Primary T*ipe2*$^{+/+}$ or *Tipe2*$^{-/-}$ macrophages were cultured in DMEM supplemented with exosome-depleted FBS. After 24 h, the conditional medium was collected for centrifugation at 3000 g for 15 min. The supernatants were used for exosome isolation by ExoQuick-TC (System Biosciences, Palo Alto, CA) according to the instructions. Briefly, the supernatants were mixed with ExoQuick-TC at a ratio of 5:1 and then incubated at room temperature overnight. After centrifugation at 1500 g for 30 min at room temperature, the pellets were resuspended as exosomes. The exosomes were identified by nanoparticle tracking analysis (ZetaView; Meerbusch, Germany). Exosomal markers TSG101 and CD63 were identified by Western blot.

Lipid ROS and cell viability assay

For lipid ROS assay, the cells were incubated with 5 μM C11-BODIPY$^{581/591}$ (Thermo Fisher Scientific, Waltham, MA) at 37 °C for 30 min away from

light, followed by flow cytometry assay or fluorescence imaging using Opera Phenix Plus High-Content Screening System (PerkinElmer, Waltham, MA). For the cellular death assay, the cells were stained with eFluor 780-conjugated fixable viability Dye (FVD; Thermo Fisher Scientific) at 4 °C for 30 min, followed by flow cytometry assay. FVD^{high} population was considered as dead cells. In some experiments, the cells were stained with Annexin V / 7-AAD Apoptosis Kit (APExBIO). And $7\text{-}AAD^{+}$ population was considered as dead cells.

Mitochondrial transfer and TNT formation assessment

To track mitochondrial transfer from macrophages to ASCs. *Tipe2*$^{+/+}$ or *Tipe2*$^{-/-}$ macrophages (2.5×10^4 per well) were labeled with 100 nM MitoTracker™ Deep Red FM (Thermo Fisher Scientific) at 37 °C for 30 min, followed by coculture with ASCs (5×10^3 per well) in a 96-well plate in the presence of FA as aforementioned. The mitochondria were tracked in ASCs through imaging with Opera Phenix Plus High-Content Screening System. To dynamically track the mitochondrial transportation, ASCs (5×10^4 per well) in coculture with MitoTracker-labeled *Tipe2*$^{-/-}$ macrophages (5×10^4 per well) in a 12-well plate were photographed for specific time periods using Long Time Live-cell Dynamic Imaging and Analysis System (Sartorius, Gottingen, Germany). In some condition, conditional medium of MitoTracker-labeled macrophages that were pretreated with GW4869 (MCE) or vehicle were collected for ASC incubation for 24 h, followed by mitochondrial tracking in ASCs. In other experiments, *Tipe2*$^{+/+}$ or *Tipe2*$^{-/-}$ macrophages (2.5×10^5 per well) were labeled with 5 μM MitoSOX (Thermo Fisher Scientific) at 37 °C for 20 min, followed by coculture with ASCs (5×10^4 per well) in a 12-well plate in the presence of FA. Mitochondrial ROS was detected in ASCs using flow cytometry.

TNT formation was examined in the coculture of ASCs and MitoTracker-labeled macrophages through staining F-actin with 5 μg/ml TRITC-conjugated phalloidin (Sigma-Aldrich) for 30 min. After fixation with 4% paraformaldehyde, fluorescence signals were examined using Opera Phenix Plus High-Content Screening System, so as to evaluate mitochondrial localization in TNTs. In some experiments, 350 nM cytochalasin B (Abcam, Cambridge, MA, UK) was used to inhibit TNT formation in the coculture of macrophages with ASCs.

Macrophage treatment and mitochondrial assessment

Primary macrophages (5×10^5 per well in a 12-well plate or 5×10^4 per well in a 96-well plate) were treated with FA (50 μM palmitate acid and 100 μM oleic acid) in conjugation BSA for indicated time period. In some condition, macrophages were treated with 50 μM Mdivi-1 (MCE) for 18 h, 10 μM BAPTA (Thermo Fisher Scientific) for 2 h, 50 μM 2-APB for 2 h, 200 nM Rapamycin (APExBIO) for 24 h or 10 μM GW4869 (MCE) for 24 h before the assessment, respectively. To detect mitochondrial ROS, macrophages were incubated with 5 μM MitoSOX for 20 min at 37 °C followed by a flow cytometry assay. In terms of mitochondrial fission assessment, macrophages were incubated with 100 nM MitoTracker for 30 min at 37 °C or performed immunofluorescence for TOMM20 using corresponding antibodies (Supplementary Table 1). Mitochondrial morphologies were examined through fluorescence imaging using Opera Phenix Plus High-Content Screening System or Dragonfly High Speed Confocal Microscope (Andor, Belfast, UK), and mitochondrial branch length was evaluated using Fiji (Fiji Is Just ImageJ) software. In other conditions, mitochondrial morphology was examined by transmission electron microscopy, and mitochondrial area was evaluated using ImageJ software.

Ferrous iron imaging

ASCs were cultured in complete DMEM plus conditioned medium from *Tipe2*$^{+/+}$ or *Tipe2*$^{-/-}$ macrophages (pretreated with FA for 18 h) at a volume ratio of 1:1 for 24 h. Intracellular Fe^{2+} was detected in ASCs using FerroOrange (Dojindo Lab, Kumamoto, Japan). Briefly, the nuclei were stained with Hoechst 33342 (Beyotime Biotechnology, Shanghai, China) at 37 °C for 10 min, followed by incubation with 1 μM FerroOrange in Hank's Balanced Salt Solution at 37 °C away from light for 30 min. Fluorescence signals were visualized using Opera Phenix Plus High-Content Screening System.

Calcium imaging and calcium flux measurement

Cytosolic free Ca^{2+} was evaluated in macrophages using fluorescent indicator Fluo-4 AM (Thermo Fisher Scientific). Briefly, the cells were incubated with 5 μM Fluo-4 AM at 37 °C for 30 min, followed by nucleus staining with Hoechst 33342 at 37 °C for 10 min. Fluorescence signals were visualized by the Opera Phenix Plus High-Content Screening System. In some experiments, macrophages were incubated with 5 μM Fluo-4 AM at 37 °C for 30 min, followed by a flow cytometry assay for Ca^{2+} flux.

Immunofluorescence

Immunofluorescence staining was performed in paraffin-embedded sections post-deparaffinization, rehydration, and antigen retrieval. Briefly, after blockade with 10% goat serum, the sections were incubated with primary antibodies overnight at 4 °C, followed by fluorochrome-conjugated secondary antibodies for 30 min at 37 °C. Nuclei were stained with DAPI. Fluorescence signals were visualized using Dragonfly High Speed Confocal Microscope. The antibodies used are listed in Supplementary Table 1.

Flow cytometry

The cells or SVF from adipose tissues were incubated with Fc block (Biolegend, San Diego, CA) at 4 °C for 15 min, followed by incubation with FITC-labeled anti-CD45 (ebioscience, clone 30-F11; Biolegend, clone 30-F11), Alexa Fluor 700-labeled anti-Sca-1 (ebioscience, clone D7) antibodies at 4 °C in dark for 30 min. For measurements of mitochondrial ROS or mitochondrial membrane potential, the cells were incubated with 5 μM MitoSOX or 100 nM MitoTracker™ Red CMXRos (Thermo Fisher Scientific) at 37 °C for 20 min before membrane molecule staining. The cells were acquired using CytoFLEX and data were analyzed by CytExpert (Beckman Coulter, Brea, CA) or FlowJo software. In some experiments, SVF from mouse VAT was stained with fluorochrome-labeled antibodies, followed by cell sorting using BD FACSAria™ II (BD Biosciences, Franklin Lakes, NJ). ASCs were identified as $Sca\text{-}1^{+}CD45^{-}$, and macrophages were identified as $CD45^{+}$ $F4/80^{+}$.

Western blot and co-immunoprecipitation

Equal amounts of protein from tissue or cell lysates were separated by SDS-PAGE and then transferred to PVDF membrane (Millipore, Billerica, MA). After blockade with 5% BSA, the membranes were incubated with primary antibodies at 4 °C overnight, followed by incubation with HRP (horseradish peroxidase)-conjugated secondary antibodies for 1 h at room temperature. The bands were visualized with an automatic chemiluminescence image analysis system (Tanon, Shanghai, China). For the co-immunoprecipitation assay, protein lysates from mouse macrophages were immunoprecipitated with antibodies against TIPE2 or IP3R, followed by immunoblotting with antibodies against IP3R and TIPE2. Equal amounts of IgG were used as negative controls. The antibodies are listed in Supplementary Table 1.

Quantitative PCR

Total RNA was extracted from the cells using the SPARKeasy Cell RNA Kit (Sparkjade®, Jinan, China), and the mRNA was transcribed into cDNA using the ReverTra Ace qPCR RT Kit (TOYOBO Life Science, Shanghai, China), according to the manufacturer's protocol. Quantitative PCR was performed using ultraSYBR Mixture (CWbiotech, Beijing, China) on CFX-Connect (Bio-Rad, Hercules, CA). The primers are listed in Supplementary Table 2.

Statistical analysis

Statistical analysis was performed with GraphPad Prism software (San Diego, CA). Statistical differences were evaluated using two-tailed student's *t*-test, one-way or two-way ANOVA. Data are expressed as the mean ± s.e.m. $P < 0.05$ is considered as significant.

Reporting summary

Further information on research design is available in the Nature Portfolio Reporting Summary linked to this article.

Data availability

Data that support the findings are provided in this manuscript. Source data are provided with this paper.

References

1. Vishvanath, L. & Gupta, R. K. Contribution of adipogenesis to healthy adipose tissue expansion in obesity. *J. Clin. Investig.* **129**, 4022–4031 (2019).
2. Ghaben, A. L. & Scherer, P. E. Adipogenesis and metabolic health. *Nat. Rev. Mol. Cell Biol.* **20**, 242–258 (2019).
3. Zhou, Z. et al. CX3CR1hi macrophages sustain metabolic adaptation by relieving adipose-derived stem cell senescence in visceral adipose tissue. *Cell Rep.* **42**, 112424 (2023).
4. Louwen, F., Ritter, A., Kreis, N. N. & Yuan, J. Insight into the development of obesity: functional alterations of adipose-derived mesenchymal stem cells. *Obes. Rev.* **19**, 888–904 (2018).
5. Jiang, X., Stockwell, B. R. & Conrad, M. Ferroptosis: mechanisms, biology and role in disease. *Nat. Rev. Mol. Cell Biol.* **22**, 266–282 (2021).
6. Stockwell, B. R. Ferroptosis turns 10: Emerging mechanisms, physiological functions, and therapeutic applications. *Cell* **185**, 2401–2421 (2022).
7. Furukawa, S. et al. Increased oxidative stress in obesity and its impact on metabolic syndrome. *J. Clin. Investig.* **114**, 1752–1761 (2004).
8. Moreno-Navarrete, J. M. & Fernández-Real, J. M. Iron: The silent culprit in your adipose tissue. *Obes. Rev.* **25**, e13647 (2023).
9. Tajima, S. et al. Iron reduction by deferoxamine leads to amelioration of adiposity via the regulation of oxidative stress and inflammation in obese and type 2 diabetes KKAy mice. *Am. J. Physiol.-Endocrinol. Metab.* **302**, E77–E86 (2012).
10. Yan, H.-F., Liu, Z.-Y., Guan, Z.-A. & Guo, C. Deferoxamine ameliorates adipocyte dysfunction by modulating iron metabolism in ob/ob mice. *Endocr. Connect.* **7**, 604–616 (2018).
11. Doll, S. et al. ACSL4 dictates ferroptosis sensitivity by shaping cellular lipid composition. *Nat. Chem. Biol.* **13**, 91–98 (2016).
12. Li, W. et al. Identifying ferroptosis-related genes associated with weight loss outcomes and regulation of adipocyte microenvironment. *Mol. Nutr. Food Res.* **67**, e2300168 (2023).
13. Eirin, A. et al. Obesity-driven mitochondrial dysfunction in human adipose tissue-derived mesenchymal stem/stromal cells involves epigenetic changes. *Cell Death Dis.* **15**, 387 (2024).
14. Nawaz, A. et al. CD206+ M2-like macrophages regulate systemic glucose metabolism by inhibiting proliferation of adipocyte progenitors. *Nat. Commun.* **8**, 286 (2017).
15. Nahmgoong, H. et al. Distinct properties of adipose stem cell subpopulations determine fat depot-specific characteristics. *Cell Metab.* **34**, 458–472.e456 (2022).
16. Shan, B. et al. Perivascular mesenchymal cells control adipose-tissue macrophage accrual in obesity. *Nat. Metab.* **2**, 1332–1349 (2020).
17. Wang, Q., Hartig, S. M., Ballantyne, C. M. & Wu, H. The multifaceted life of macrophages in white adipose tissue: Immune shift couples with metabolic switch. *Immunological Rev.* **324**, 11–24 (2024).
18. Zhao, H. et al. Exosomes from adipose-derived stem cells attenuate adipose inflammation and obesity through polarizing m2 macrophages and beiging in white adipose tissue. *Diabetes* **67**, 235–247 (2018).
19. Nance, S. A., Muir, L. & Lumeng, C. Adipose tissue macrophages: Regulators of adipose tissue immunometabolism during obesity. *Mol. Metab.* **66**, 101642 (2022).
20. Chavakis, T., Alexaki, V. I. & Ferrante, A. W. Macrophage function in adipose tissue homeostasis and metabolic inflammation. *Nat. Immunol.* **24**, 757–766 (2023).
21. Orr, J. S. et al. Obesity alters adipose tissue macrophage iron content and tissue iron distribution. *Diabetes* **63**, 421–432 (2014).
22. Wang, Z. et al. TIPE2 protein serves as a negative regulator of phagocytosis and oxidative burst during infection. *Proc. Natl Acad. Sci. USA.* **109**, 15413–15418 (2012).
23. Li, W. et al. TNFAIP8L2/TIPE2 impairs autolysosome reformation via modulating the RAC1-MTORC1 axis. *Autophagy* **17**, 1410–1425 (2020).
24. Bi, J. et al. TIPE2 is a checkpoint of natural killer cell maturation and antitumor immunity. *Sci. Adv.* **4**, eabi6515 (2021).
25. Sun, H. et al. TIPE2 controls innate immunity to rna by targeting the phosphatidylinositol 3-kinase–rac pathway. *J. Immunol.* **189**, 2768–2773 (2012).
26. Sun, H. et al. TIPE2, a negative regulator of innate and adaptive immunity that maintains immune homeostasis. *Cell* **133**, 415–426 (2008).
27. Tao, Y. et al. Hepatocyte TIPE2 is a fasting-induced Raf-1 inactivator that drives hepatic gluconeogenesis to maintain glucose homeostasis. *Metabolism* **148**, 155690 (2023).
28. Yang, Y. et al. TIPE2 knockout reduces myocardial cell damage by inhibiting IFN-γ-mediated ferroptosis. *Biochimica et. Biophysica Acta (BBA) - Mol. Basis Dis.* **1869**, 166566 (2023).
29. Eckel-Mahan, K., Ribas Latre, A. & Kolonin, M. G. Adipose Stromal Cell Expansion and Exhaustion: Mechanisms and Consequences. *Cells* **9**, 863 (2020).
30. Höhn, A., Jung, T., Grimm, S. & Grune, T. Lipofuscin-bound iron is a major intracellular source of oxidants: Role in senescent cells. *Free Radic. Biol. Med.* **48**, 1100–1108 (2010).
31. Li, T. et al. Genome-wide analysis reveals TNFAIP8L2 as an immune checkpoint regulator of inflammation and metabolism. *Mol. Immunol.* **99**, 154–162 (2018).
32. Maniyadath, B., Zhang, Q., Gupta, R. K. & Mandrup, S. Adipose tissue at single-cell resolution. *Cell Metab.* **35**, 386–413 (2023).
33. Lou, Y. et al. The SCFβ-TrCP E3 Ubiquitin Ligase Regulates Immune Receptor Signaling by Targeting the Negative Regulatory Protein TIPE2. *J. Immunol.* **204**, 2122–2132 (2020).
34. Goldsmith, J. R. & Chen, Y. H. Regulation of inflammation and tumorigenesis by the TIPE family of phospholipid transfer proteins. *Cell. Mol. Immunol.* **14**, 482–487 (2017).
35. Sakers, A., De Siqueira, M. K., Seale, P. & Villanueva, C. J. Adipose-tissue plasticity in health and disease. *Cell* **185**, 419–446 (2022).
36. Gimble, J., Rigamonti, A., Brennand, K., Lau, F. & Cowan, C. A. Rapid Cellular Turnover in Adipose Tissue. *PLoS ONE* **6**, e17637 (2011).
37. Neese, R. A. et al. Measurement in vivo of proliferation rates of slow turnover cells by 2H2O labeling of the deoxyribose moiety of DNA. *Proc. Natl Acad. Sci. USA* **99**, 15345–15350 (2002).
38. Komegae, E. N. et al. Site-specific reprogramming of macrophage responsiveness to bacterial lipopolysaccharide in obesity. *Front. Immunol.* **10**, 1496 (2019).
39. Cochain, C. et al. Single-cell RNA-seq reveals the transcriptional landscape and heterogeneity of aortic macrophages in murine atherosclerosis. *Circulation Res.* **122**, 1661–1674 (2018).
40. Embgenbroich, M. et al. Soluble mannose receptor induces proinflammatory macrophage activation and metaflammation. *Proc. Natl Acad. Sci.* **118**, e2103304118 (2021).

41. Truman-Rosentsvit, M. et al. Ferritin is secreted via 2 distinct non-classical vesicular pathways. *Blood* **131**, 342–352 (2018).
42. Borcherding, N. & Brestoff, J. R. The power and potential of mitochondria transfer. *Nature* **623**, 283–291 (2023).
43. Tiash, S., Brestoff, J. R. & Crewe, C. A guide to studying mitochondria transfer. *Nat. Cell Biol.* **25**, 1551–1553 (2023).
44. Saha, T. et al. Intercellular nanotubes mediate mitochondrial trafficking between cancer and immune cells. *Nat. Nanotechnol.* **17**, 98–106 (2021).
45. Cereghetti, G. M. et al. Dephosphorylation by calcineurin regulates translocation of Drp1 to mitochondria. *Proc. Natl Acad. Sci. USA* **105**, 15803–15808 (2008).
46. Giacomello, M., Pyakurel, A., Glytsou, C. & Scorrano, L. The cell biology of mitochondrial membrane dynamics. *Nat. Rev. Mol. Cell Biol.* **21**, 204–224 (2020).
47. Kalia, R. et al. Structural basis of mitochondrial receptor binding and constriction by DRP1. *Nature* **558**, 401–405 (2018).
48. Thillaiappan, N. B., Smith, H. A., Atakpa-Adaji, P. & Taylor, C. W. KRAP tethers IP3 receptors to actin and licenses them to evoke cytosolic Ca2+ signals. *Nat. Commun.* **12**, 4514 (2021).
49. Vatner, D. F. et al. Insulin-independent regulation of hepatic triglyceride synthesis by fatty acids. *Proc. Natl Acad. Sci.* **112**, 1143–1148 (2015).
50. Azzu, V., Vacca, M., Virtue, S., Allison, M. & Vidal-Puig, A. Adipose Tissue-Liver Cross Talk in the Control of Whole-Body Metabolism: Implications in Nonalcoholic Fatty Liver Disease. *Gastroenterology* **158**, 1899–1912 (2020).
51. Bo, T. et al. Hepatic selective insulin resistance at the intersection of insulin signaling and metabolic dysfunction-associated steatotic liver disease. *Cell Metab.* **36**, 947–968 (2024).
52. Goldrick, R. B. & McLoughlin, G. M. Lipolysis and lipogenesis from glucose in human fat cells of different sizes. *J. Clin. Investig.* **49**, 1213–1223 (1970).
53. Kubota, T. et al. Downregulation of macrophage Irs2 by hyperinsulinemia impairs IL-4-indeuced M2a-subtype macrophage activation in obesity. *Nat. Commun.* **9**, 4863 (2018).
54. Adamson, S. E. et al. Disabled homolog 2 controls macrophage phenotypic polarization and adipose tissue inflammation. *J. Clin. Investig.* **126**, 1311–1322 (2016).
55. Jackson, M. V. et al. Mitochondrial transfer via tunneling nanotubes is an important mechanism by which mesenchymal stem cells enhance macrophage phagocytosis in the in vitro and in vivo models of ARDS. *Stem Cells* **34**, 2210–2223 (2016).
56. Islam, M. N. et al. Mitochondrial transfer from bone-marrow–derived stromal cells to pulmonary alveoli protects against acute lung injury. *Nat. Med.* **18**, 759–765 (2012).
57. Nicolás-Ávila, J. A. et al. A network of macrophages supports mitochondrial homeostasis in the heart. *Cell* **183**, 94–109.e123 (2020).
58. Rosina, M. et al. Ejection of damaged mitochondria and their removal by macrophages ensure efficient thermogenesis in brown adipose tissue. *Cell Metab.* **34**, 533–548.e512 (2022).
59. Yang, J. et al. Highly-purified rapidly expanding clones, RECs, are superior for functional-mitochondrial transfer. *Stem Cell Res. Ther.* **14**, 40 (2023).
60. Crewe, C. et al. Extracellular vesicle-based interorgan transport of mitochondria from energetically stressed adipocytes. *Cell Metab.* **33**, 1853–1868.e1811 (2021).
61. Todkar, K. et al. Selective packaging of mitochondrial proteins into extracellular vesicles prevents the release of mitochondrial DAMPs. *Nat. Commun.* **12**, 1971 (2021).
62. Harrison, P. M. & Arosio, P. The ferritins: molecular properties, iron storage function and cellular regulation. *Biochim Biophys. Acta* **1275**, 161–203 (1996).
63. Honarmand Ebrahimi, K., Bill, E., Hagedoorn, P.-L. & Hagen, W. R. The catalytic center of ferritin regulates iron storage via Fe(II)-Fe(III) displacement. *Nat. Chem. Biol.* **8**, 941–948 (2012).
64. Yanatori, I., Nishina, S., Kishi, F. & Hino, K. Newly uncovered biochemical and functional aspects of ferritin. *FASEB J.* **37**, e23095 (2023).
65. Fuhrmann, D. C., Mondorf, A., Beifuß, J., Jung, M. & Brüne, B. Hypoxia inhibits ferritinophagy, increases mitochondrial ferritin, and protects from ferroptosis. *Redox Biol.* **36**, 101670 (2020).
66. Hou, W. et al. Autophagy promotes ferroptosis by degradation of ferritin. *Autophagy* **12**, 1425–1428 (2016).
67. Zhang, Y. et al. mTORC1 couples cyst(e)ine availability with GPX4 protein synthesis and ferroptosis regulation. *Nat. Commun.* **12**, 1589 (2021).
68. Xia, W. et al. Obesity causes mitochondrial fragmentation and dysfunction in white adipocytes due to RalA activation. *Nat. Metab.* **6**, 273–289 (2024).
69. Ikeda, Y. et al. Deletion of H-ferritin in macrophages alleviates obesity and diabetes induced by high-fat diet in mice. *Diabetologia* **63**, 1588–1602 (2020).
70. Markelic, M. et al. The origin of lipofuscin in brown adipocytes of hyperinsulinaemic rats: the role of lipid peroxidation and iron. *Histol. Histopathol.* **28**, 493–503 (2013).

Acknowledgements

We thank Advanced Medical Research Institute and Translational Medicine Core Facility of Shandong University for providing Microscopy Characterization Facility. We thank The Second Hospital of Shandong University for providing nanoparticle tracking analysis, and Central Hospital Affiliated to Shandong First Medical University for providing transmission electron microscopy. This work was supported by National Natural Science Foundation of China (Grant 82471774, 81970733 to Q.W.) and Shandong Provincial Natural Science Foundation of China (Grant ZR2023ZD55, ZR2024MH120 to Q.W., ZR2023QH184 to H.Z.).

Author contributions

Y.T. designed and performed the study, prepared the original draft. J.Z. and T.W. performed experiments. P.S. and H.J. analyzed data. Z.Z., H.L., Y.W., Y.L., and M.K. assisted in animal experiments. H.Z., F.W., S.D., C.G., F.Z., H.M., F.L., and L.Z. provided technical assistance, key resources, and data interpretation. Q.W. conceived and supervised the study, wrote the manuscript.

Competing interests

The authors declare no competing interests.

Additional information

Supplementary information The online version contains supplementary material available at https://doi.org/10.1038/s41467-025-62690-1.

Correspondence and requests for materials should be addressed to Qun Wang.

Peer review information *Nature Communications* thanks the anonymous reviewers for their contribution to the peer review of this work. A peer review file is available.